



# Recent activity and paleoseismicity of an intraplate extensional fault: the Calamocha fault (Jiloca graben, central Iberian Chain)

Alba Peiro<sup>1</sup> · José L. Simón<sup>1</sup> · Leticia Martín-Bello<sup>1</sup> · Luis E. Arlegui<sup>1</sup> · Lope Ezquerro<sup>1</sup> · Aránzazu Luzón<sup>1</sup> · Alicia Medialdea<sup>2</sup> · Belén Corral<sup>1</sup> · Carlos L. Liesa<sup>1</sup>

Received: 23 May 2022 / Accepted: 24 October 2022 / Published online: 25 November 2022  
© The Author(s) 2022

## Abstract

The Calamocha fault is an 18-km-long, NNW–SSE striking pure normal fault that moves down the northern sector of the Jiloca graben with respect to the Neogene infill of the Calatayud basin (central Iberian Chain). Its structure and kinematics are characterized by means of detailed geological mapping, morphotectonic analysis and data recording at the outcrop scale. The Calamocha fault represents the inversion of a previous contractional fault zone under the recent tensional stress field (WSW–ENE trending  $\sigma_3$  trajectories). The extensional activity started during the Late Pliocene (ca. 3.8 Ma), accumulating a maximum net slip of 190–230 m (long-term slip rate of 0.05–0.06 mm/a). The palaeoseismological study of three artificial exposures near Calamocha town evidenced recurrent slip during the Late Pleistocene, which proves its active character. Analysis of faulted clastic alluvial units, dated by means of optically stimulated luminescence (OSL), reveals at least eight slip events since  $145.9 \pm 9.1$  ka, the last one being younger than  $13.8 \pm 0.9$  ka. Only a few events represent visible accumulated displacement on the main synthetic rupture surfaces; this allows a rough estimate of the short-term slip rate (during the Late Pleistocene) of about 0.1 mm/a, faster than the long-term rate. The Calamocha fault could potentially produce a characteristic earthquake (in the sense of Schwartz and Coppersmith, J Geophys Res 89:5681–5698, 1984) with moment magnitude  $M_w \approx 6.7 \pm 0.3$  ( $M_w \approx 6.9 \pm 0.3$  in a scenario of activation of the whole Calamocha–Daroca fault zone), average coseismic displacement of 0.5–1.3 m and average recurrence period under 15 ka.

**Keywords** Normal fault · Slip rate · Trench study · OSL dating · Morphotectonics · Late Pleistocene

✉ José L. Simón  
jsimon@unizar.es

Alba Peiro  
apeiro@unizar.es

Leticia Martín-Bello  
leticia.martin.bello@gmail.com

Luis E. Arlegui  
arlegui@unizar.es

Lope Ezquerro  
lopezquerro@gmail.com

Aránzazu Luzón  
aluzon@unizar.es

Alicia Medialdea  
alicia.medialdea@cenieh.es

Belén Corral  
riveraesvida@gmail.com

Carlos L. Liesa  
carluis@unizar.es

<sup>1</sup> Dpto. de Ciencias de la Tierra, Grupo Geotransfer-Instituto Universitario de Investigación en Ciencias Ambientales de Aragón (IUCA), Universidad de Zaragoza, Pedro Cerbuna 12, 50009 Saragossa, Spain

<sup>2</sup> Centro Nacional de Investigación sobre la Evolución Humana (CENIEH), Paseo Sierra de Atapuerca 3, 09002 Burgos, Spain

## Introduction

Intraplate regions usually exhibit low to moderate seismicity, and their active faults have large return periods (in the order of  $10^3$  years; Liu and Zoback 1997), which means that they tend to be underestimated in seismic hazard analyses. Therefore, it is critical to study the geological record for identifying and dating large ancient earthquakes by means of palaeoseismological methods (Allen 1986; McCalpin 2009; Yeats et al. 1997). Such is the case of the Iberian Chain, in the eastern Iberian Peninsula (Fig. 1a, b), a region that exhibits low to moderate historical and instrumental seismicity, but contains numerous slow active normal faults. Among the latter, those located at the junction of the Teruel and Jiloca grabens (Sierra Palomera, Concud, Teruel and Valdecebro faults) have been the focus of a number of detailed palaeoseismological studies during the last decade, which have demonstrated their Pleistocene activity and seismogenic potential (Lafuente et al. 2011, 2014; Simón et al. 2012, 2016, 2017; 2019; Ezquerro et al. 2015, 2016; Peiro et al. 2020, 2022).

The Calamocha fault is a NNW–SSE striking normal fault that brings into contact the Neogene units of the Calatayud basin with the Pleistocene sediments that infill the northern sector of the Jiloca graben (Fig. 1c). Together with the Daroca fault, they define a conspicuous extensional fault zone along the central Iberian Chain. Contractive structures have also been reported along this fault zone, mostly in the surrounding area of Daroca town (Daroca thrust; Colomer and Santanach 1988; Casas et al. 2018; Simón et al. 2021) and the area NW of Calamocha (Corral 2014; Liesa et al. 2021). This suggests a compressional origin for the overall structure, probably due to Alpine reactivation of a Variscan fault that formed the SW boundary of the Calatayud basin. During Plio-Quaternary times, its inversion gave rise to the Calamocha–Daroca normal fault zone.

The Calamocha fault shows signs of Quaternary activity, already noticed by Simón (1983), and documented in detail by Simón et al. (2012) and Martín-Bello et al. (2014). It has been incorporated into the national database of active faults created by IGME (Instituto Geológico y Minero de España), but no exhaustive palaeoseismic research aiming

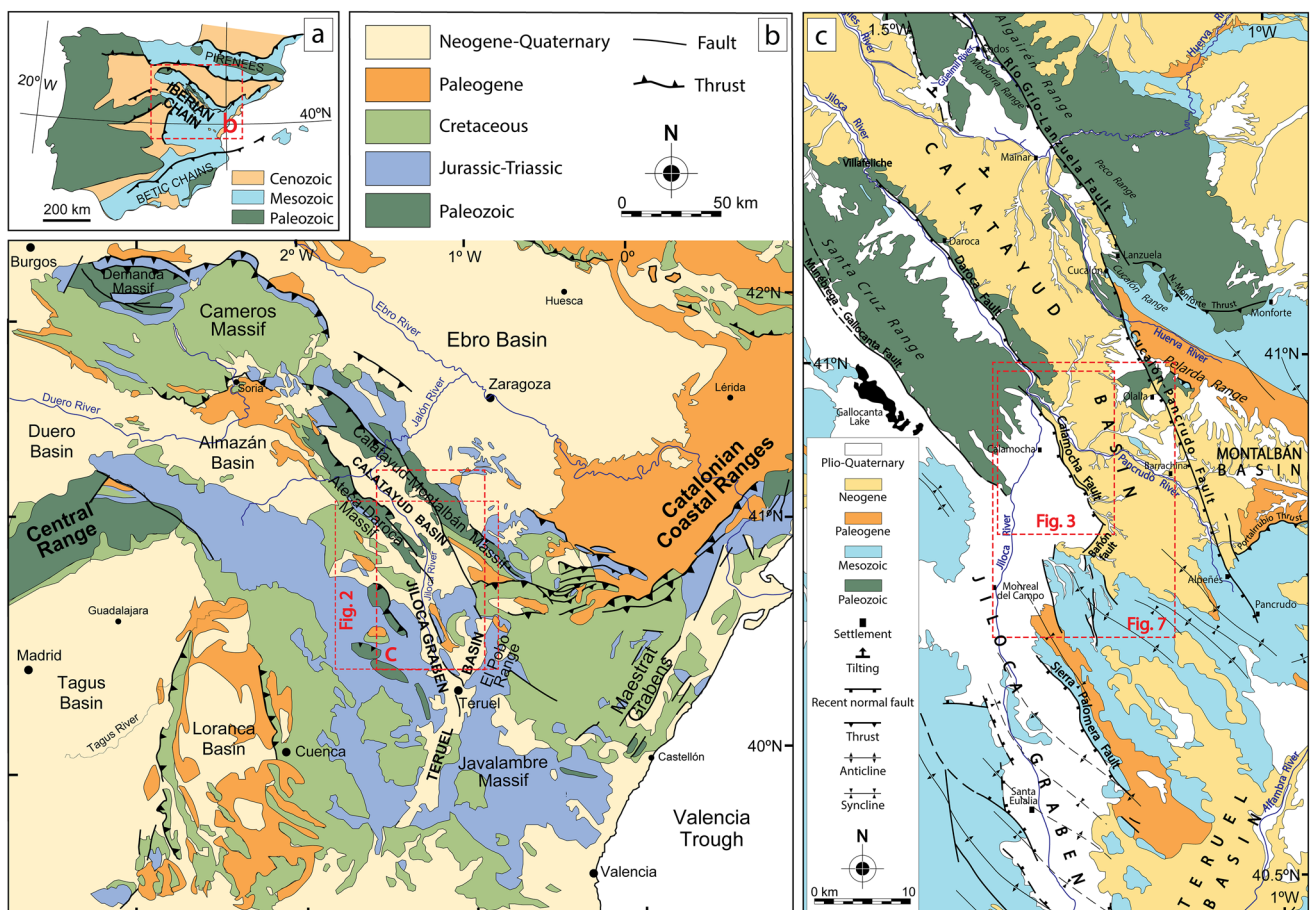


**Fig. 1** a Location of the Iberian Chain within the Iberian Peninsula. b Geological sketch of the Iberian Chain, with location of the main Neogene–Quaternary extensional basins. c Simplified geological map of the Calatayud and Jiloca basins, with location of Figs. 2, 4 and 8

to reconstruct its recent faulting history has been conducted yet.

The objective of this paper is to document the structure and recent activity of the Calamocha fault. In particular, its geometry, kinematics and evolution are characterized, including an estimate of long-term and short-term slip rates. Moreover, some rupture events dated to the Pleistocene have been identified from palaeoseismological analysis of a number of artificial exposures in the vicinity of Calamocha. In this way, we aim to contribute to an overall understanding of extensional tectonic processes in the central–eastern Iberian Chain during Neogene and Quaternary times.

## Geological setting

### Overall view

The Iberian Chain is a NW–SE trending, intraplate mountain chain located within the Iberian Peninsula (Fig. 1a, b), which developed during Cenozoic time owing to its convergence with both the European and African plates (Álvaro et al. 1979; Capote et al. 2002). The chain mainly resulted from the inversion of several Mesozoic basins (Liesa et al. 2018) during compressional episodes of the Alpine Orogeny (Palaeogene to early Neogene; Liesa and Simón 2009). Within the central sector of the chain, an up to 11,000 m thick Palaeozoic sequence was re-folded during the Cenozoic compression, the macrostructures exhibiting a prevalent NW–SE trend (Cortés-Gracia and Casas-Sainz 1996; Calvín-Ballester and Casas 2014). In this sector, two large, Palaeozoic structural highs, the Calatayud–Montalbán and the Ateca–Daroca massifs, each one with wavelength of about 25 km and estimated amplitude of 2 km (Casas et al. 2016), are separated by the Cenozoic Calatayud basin (Fig. 1c).

Since the beginning of the Late Miocene, the central–eastern Iberian Chain underwent an extensional tectonic period linked to rifting of the Valencia Trough (Vegas et al. 1979; Simón 1982; Roca and Guimerà 1992; Mailard and Mauffret 1999). Onshore extensional deformation has been accommodated by normal faults that bound large Neogene–Quaternary basins (Maestrat, Teruel, Jiloca, Gallocanta, Munébrega), and mostly represent the inversion of previous compressional faults (Álvaro et al. 1979).

Two extensional stages, Late Miocene to Early Pliocene and Late Pliocene–Quaternary, have traditionally been distinguished (Moissenet, 1980; Simón, 1982, 1983, 1989; Anadón and Moissenet, 1996; Ezquerro et al., 2020). They are characterized by two distinct tensional stress fields ( $\sigma_1$  vertical): (i) uniaxial tension with WNW–ESE trending  $\sigma_3$  trajectories, prevailing during the first episode; (ii) nearly radial tension ( $\sigma_2 \approx \sigma_3$ ) with  $\sigma_3$  trajectories trending

WSW–ENE, prevailing during the second episode (Simón 1982, 1989; Arlegui et al. 2005; Liesa et al. 2019). The latter has essentially remained until the present day (Herraiz et al. 2000). The overall NNW–SSE trend of the Jiloca graben, developed during the second extensional episode, constitutes the most conspicuous macrostructural expression of the regional stress trajectories (Simón 1989). Besides, the oblique, NW–SE striking individual faults resulting from inversion of Palaeogene thrusts represent the structural inheritance.

### The Mio-Pliocene Calatayud basin

The NW–SE trending, 65-km-long Calatayud basin, developed in a compressional setting bounded by the Palaeozoic Ateca–Daroca and the Calatayud–Montalbán massifs (Fig. 1c). In particular, the SW margin corresponds to the Daroca thrust, where Cambrian rocks overthrust the Lower Miocene continental deposits of the basin infill, while younger, Middle–Upper Miocene units overlap the thrust front from the SW margin of the basin (Julivert 1954; Colomer and Santanach 1988; Casas et al. 2018; Liesa et al. 2021; Simón et al. 2021).

Subsidence within the Calatayud basin developed in a complex compressional–extensional setting during the entire Neogene, allowing the accumulation of the most complete Neogene series in the Iberian Chain (Anadón et al. 2004). The sedimentary record consists of clastic alluvial sediments sourced at the basin margins, which grades towards central sectors into lacustrine–palustrine evaporites and carbonates (Gabaldón et al. 1991; Sanz-Rubio 1999; Sanz-Rubio et al. 2003).

Several non-formal lithostratigraphic units were distinguished within the Neogene series of the south-eastern sector of the Calatayud basin by Hernández et al. (1983), then adapted by Martín-Bello et al. (2014):

- The Daroca clastic unit (CU; late Aagenian–middle Aragonian), made of siliceous gravel and silt, is divided into three subunits (CU1, CU2 and CU3) based on its vertical relationships with the carbonate units.
- Navarrete gypsum (NG; early Aragonian).
- The carbonate succession of the Bañón unit-Nombrevilla limestone (NL; Aragonian) is separated into two subunits (NL1 and NL2) by the clastic unit CU2.
- Rojo 1 (R1; Vallesian-Turolian) is made of red siltstone with interbedded gravel and sandstone
- Páramo 1 (P1; Turolian) is made of limestone and marl.
- Rojo 2 (R2) and Páramo 2 (P2) (Ruscian) consist of red siltstone and marly limestone, respectively, the latter culminating the endorheic sedimentary succession of the Calatayud basin. Within the Calamocha fault

domain, both units only crop out in the hanging-wall block.

- Rojo 3 (R3; Ruscinian–Villafranchian) is made up of red mudstone with interbedded sandstone and siliceous gravel.

### Plio-Quaternary normal faults linked to the Calatayud basin

Under the Plio-Quaternary extensional regime, some of the thrusts that bound the Calatayud basin were inverted. The NE margin of the Calatayud basin is now partially controlled by the Río Grío–Pancrudo normal fault zone (Gutiérrez et al. 2013; Peiro and Simón 2021a, b), while its SW margin is represented by the Munébrega–Gallocanta (Gutiérrez et al. 2009) and the Daroca–Calamocha normal fault zones (Gracia 1992; Gutiérrez et al. 2008, 2020a; Fig. 1c). The present-day structure represents a stepped array of half-grabens, with their respective faults at their north-eastern margins.

Normal slip along the NNW–SSE trending extensional Río Grío–Pancrudo Fault Zone has produced a vertical displacement of 300 m in a late Neogene planation surface (FES3; “[Morphotectonic evolution: late neogene planation surfaces](#)”, hanging-wall tilting, and subsequent drainage reversal after the Pliocene–Pleistocene transition (Peiro and Simón 2021a, b). Surficial faulting of Late Pleistocene materials has provided a slip rate approaching 0.30–0.36 mm/a (Peiro and Simón 2021b).

The Munébrega–Gallocanta fault zone bounds the Munébrega Plio-Quaternary, NW–SE trending half-graben, as well as the endorheic Gallocanta lacustrine basin (Gracia et al. 2002; Gutiérrez et al. 2008). Offset of a Late Pleistocene pediment has provided a vertical slip rate in the range of 0.02–0.10 mm/a (Gutiérrez et al. 2009, 2020b).

The recent Daroca–Calamocha fault zone bounds the northern sector of the Jiloca graben and the Daroca half-graben with respect to the Neogene infill of the Calatayud basin (Julivert 1954; Gracia 1992; Gutiérrez et al. 2008; Fig. 1c). Most of the Calatayud basin lies at its footwall block, but small portions of its Neogene infill were sunk and covered by Plio-Pleistocene deposits in the Jiloca basin. The fault zone is made up of two NNW–SSE to NW–SE trending segments (Daroca and Calamocha faults, 27 and 18 km long, respectively), connected by a right-stepping relay zone 1.8 km wide. The normal Daroca fault forms the north-eastern margin of the Daroca half-graben and tilts its Upper Pliocene–Pleistocene infill. A vertical slip rate of 0.02–0.06 mm/a has been estimated from the offset of a Pleistocene erosional–aggradation pediment, with the youngest event being dated to 2354–1544 cal yr BP (Gutiérrez et al. 2020a).

### The Jiloca graben

The Calamocha fault, together with the Sierra Palomera and Concud faults, form the eastern boundary of the asymmetric Jiloca graben (Fig. 1c). They show an en-échelon, right-stepping arrangement that results in an NNW–SSE trend for the overall basin. A number of Palaeogene folds are obliquely cut by the graben; nevertheless, they are nearly parallel to the Sierra Palomera and Concud faults, which also represent the inversion of Palaeogene contractional faults (Lafuente et al. 2011; Simón et al. 2021).

The Sierra Palomera fault is a 15.5-km-long, NNW–SSE striking normal fault with a nearly pure normal sense of slip. Its activity since Late Pliocene times is mainly revealed by the tilting and offset of regional planation surfaces, which allows the estimation of a throw in the range of 350–400 m (Rubio and Simón 2007; García-Lacosta et al. 2014; Peiro et al. 2022). A subsidiary antithetic fault, induced by rollover bending associated with the Sierra Palomera fault, shows evidence of recurrent activity during Late Pleistocene times (Peiro et al. 2022).

The relay zone between the Calamocha and the Sierra Palomera faults is controlled by the NE–SW striking Bañón fault (Fig. 1c), an incipient connecting fault that is unlikely to evolve into a complete hard linkage. Instead, recent deformation within the relay zone is mainly accommodated by distributed along-strike minor faults, controlled by both the regional stress field and the structural inheritance (Peiro et al. 2020). As of today, the Calamocha and Sierra Palomera faults behave as independent structures from the geometrical and kinematical point of view (Peiro et al. 2020).

The Jiloca basin infill is made of an Upper Pliocene–Pleistocene alluvial succession, in which two units are distinguished: (i) a Villafranchian pediment (V) represents an alluvial system covering wide sectors of the hanging wall, made up of several metres to several tens of metres of red gravel and silt; (ii) Quaternary sediments mostly correspond to alluvial systems made up of unconsolidated polygenetic gravel associated with the fault scarp, although palustrine lutites and carbonates are also recognized in local endorheic areas (Cañizar lake; Rubio 2004; Rubio et al. 2007).

### Morphotectonic evolution: late Neogene planation surfaces

Mountains surrounding the Jiloca basin show extensive erosion surfaces developed through successive planation episodes, which model Palaeozoic, Mesozoic and Palaeogene rocks and level compressional structures. The main planation surface, classically referred to as *Fundamental Erosion Surface* (FES; Peña et al. 1984), has recently been divided into three sublevels, FES upper sublevel (FES1), FES *s.s.* (FES2) and FES lower sublevel (FES3)



(Simón-Porcar et al. 2019; Ezquerro et al. 2020). FES2 and FES3 are probably equivalent to the S1 and S2 surfaces, respectively, defined by Gutiérrez and Gracia (1997).

Physical correlation of such sublevels with distinct sedimentary horizons of the Teruel basin made it possible for them to be dated precisely, based on robust biostratigraphic and magnetostratigraphic data (Ezquerro 2017; Ezquerro et al. 2020). The age of FES3 (3.5 Ma) is well constrained to the top of the M8 megasequence defined by Ezquerro (2017), equivalent to the upper part of Páramo 2 unit (Early Villafranchian; mammal biozone MN16; near the base of chron C2An.3n), while FES 1 and FES2 merge into the top of M7 (3.8 Ma; lower part of Páramo 2 unit; Late Ruscinian; MN15; middle part of C2Ar) (Ezquerro et al. 2020).

FES3 is either locally incised by a lower erosional surface (FES4), or overlaid by the Rojo 3 unit (R3) and the *Villafranchian pediments* that extend over most of the Jiloca basin and its margins. The associated Villafranchian alluvial system is dated to the earliest Pleistocene by macromammal fauna (Adrover 1986; MN17 zone, 2.6–1.9 Ma) and, more accurately, by magnetostratigraphy (1.95–2.1 Ma; Sinusía et al. 2004). Development of this pediment system represented the transition to external drainage in the whole region, except for certain sectors in which endorheic conditions remained until the Early Pleistocene (Teruel area; Ezquerro et al. 2012) or even until historical and present times (Gallocanta lake; Cañizar lake, Rubio and Simón 2007).

## Seismicity

Historic and instrumental seismicity of the region is low to moderate. The epicentres are clustered: (i) close to the margins of the southern Jiloca graben; (ii) in the Albarracín massif, with a maximum intensity of VI–VII at Orihuela del Tremedal (1848) (IGN 2022), and (iii) along the Molina de Aragón plateau (Fig. 2). Nevertheless, the most recent and strong earthquakes have been recorded north of those domains, west of Daroca: Cimballa (1912; intensity VI–VII) and Used (1953; intensity VII; magnitude 4.7) (IGN 2022). Earthquakes located at the Calatayud basin and its active bounding fault zones are very scarce. Focal depths typically range from 5 to 15 km, which corresponds to the brittle layer above the basal detachment level identified by Roca and Guimerà (1992). Most of the available focal mechanisms correspond to normal faults and are consistent with the regional active stress field (Herraiz et al. 2000).

## Methods

### Structural and morphotectonic study

The structure of the Calamocha fault zone has been characterized by means of a detailed geological map,

elaborated with the help of published maps at a 1:50,000 scale (Hernández et al. 1983), aerial photographs at a 1:30,000 scale, satellite orthoimages, digital elevation models (DEM, pixel = 2 m) and the resulting hillshade images, and field survey. Three geological cross sections through the northern, central and southern sector of the Calamocha fault were constructed based on mapping and outcrop information, partially inspired by those of Martín-Bello et al. (2014), Corral (2014), and Liesa et al. (2021).

Recent structures have also been analysed on a morphotectonic map, elaborated from photogeological and DEM studies, which includes remnants of the Late Neogene planation surfaces (sublevels FES1 to FES4 of the *Fundamental Erosion Surface*). Among them, the most extensively represented (FES2 and FES3) have been used as geomorphological markers of recent deformation. Their topographical reconstruction (height contours) and dating (“*Morphotectonic evolution: late neogene planation surfaces*”) have provided tools for calculating the maximum displacement and the long-term slip rate for the Calamocha fault.

### Palaeoseismological study

Direct palaeoseismological and structural data at outcrop scale contribute to characterize the geometry and kinematics of the Calamocha fault. Three fresh artificial slopes adjacent to civil constructions have been investigated following the procedure proposed by McCalpin (2009): Zaragoza–Sagunto Railway (ZSR), Polígono Agroalimentario (PA), and A-23 highway (A23H). Slopes displaying the best palaeoseismic information were cleaned, equipped with a square grid (0.5–3 m on each side, depending on the overall dimensions of each section and the level of detail required), and logged with sketches and detailed photographs. Sedimentary units and structures were marked after being classified based on characteristics such as colour, grain size, composition and texture.

Analysis of the relationships between sedimentary units and faults have allowed the reconstruction of deformation episodes, and hence to chronologically constrain palaeoseismic events. Depending on whether the slip vector is known or not, either the net slip or the throw (vertical separation of a marker) is estimated on each individual fault. Throw values are reliable for horizontal markers, while calculations of net slip are only approximate in most cases owing to the lack of information on fault kinematics. Another source of error in reconstructing the geometry of structures is the fact that the surveyed artificial exposures are not vertical but dipping slopes. Detailed logs of such slopes are projected into vertical planes, but they are not equivalent to true vertical sections.

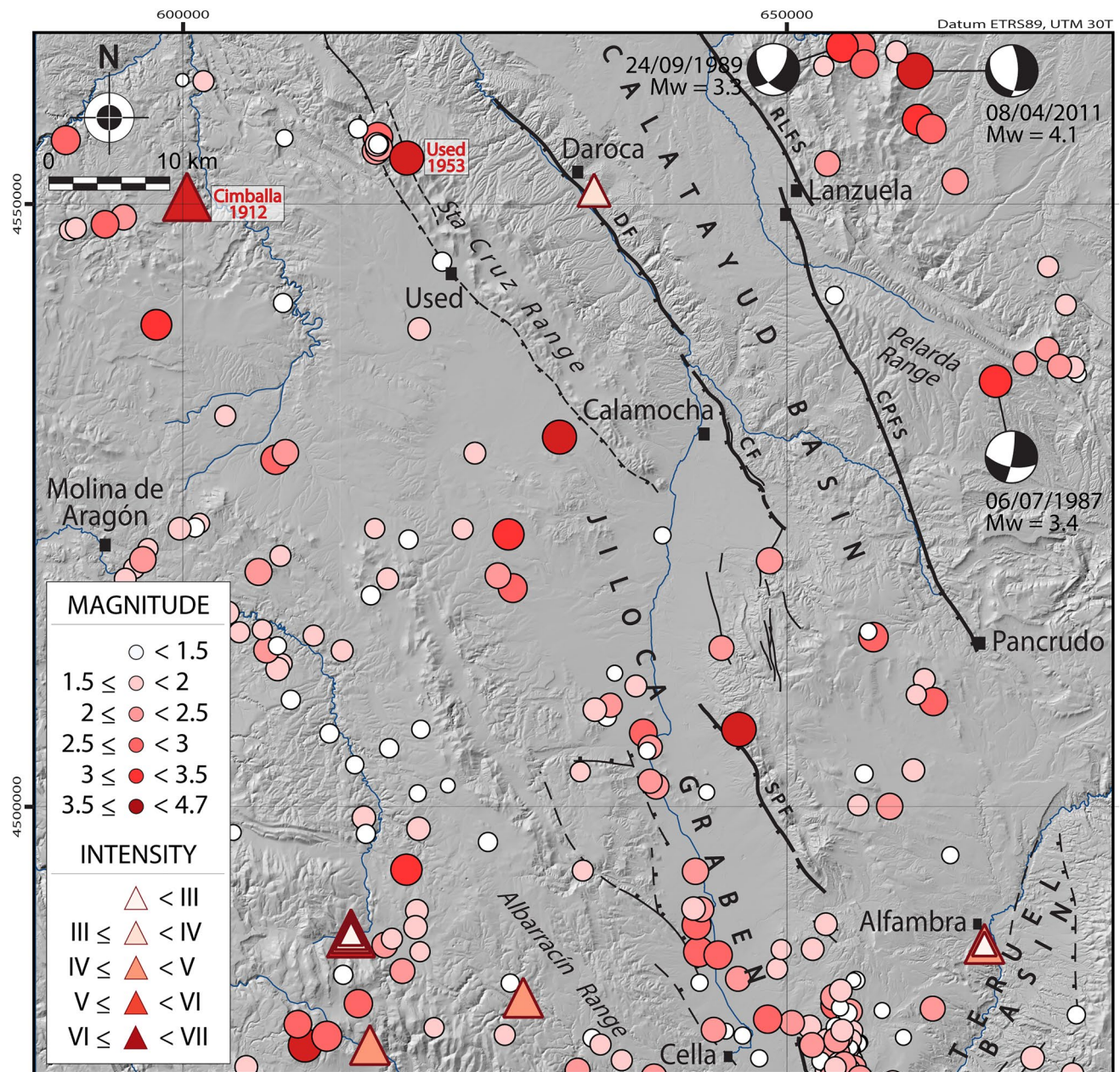


**Fig. 2** Epicentre map of historic and instrumental earthquakes in the central Iberian Chain (data source: IGN 2022). *RLFS* Río Grío–Lanzuela fault, *CPFS* Cucalón–Pancrudo fault, *DF* Daroca fault, *CF* Calamocha fault

## OSL dating

Because of the lack of organic matter samples, the sedimentary units were dated using the optically stimulated luminescence (OSL) method. A total of 16 samples of fine clastic sediments were collected using opaque tubes to avoid exposure to daylight.

Ten samples were collected during a field campaign in 2019 at the main surveyed trench (ZSR), then processed by

the Luminescence Dating Laboratory of CENIEH (Burgos, Spain). They were treated under controlled light conditions following standard procedures (Wintle 1997) to extract the quartz grains of sizes 180–250  $\mu\text{m}$ . The procedure involved: (i) treatment with HCl and  $\text{H}_2\text{O}_2$  to remove carbonates and organic matter, respectively; (ii) density separation isolating the fraction between 2.62 and 2.7  $\text{g}/\text{cm}^3$ ; and (iii) treatment with HF 40% for 50 min to dissolve any possible remaining feldspar and to etch the outer layer of the quartz grains.



Luminescence measurements were carried out in an automated Risø OSL/TL reader (TL-DA 20). Dose distributions derived from the measurement of 48–60 multigrain aliquots per sample were reduced by excluding the identified outliers; outliers have been defined as those values out of 1.5 times outside of the interquartile range. Central age model (CAM, Galbraith et al. 1999) on the reduced distributions was used to estimate the burial dose of each sample.

Environmental dose rates were calculated from the contribution of beta, gamma and cosmic radiation. Beta and gamma were based on the radionuclide concentration measured at the Centro de Investigación, Tecnología e Innovación (CITIUS) of the University of Sevilla by using a hyperpure germanium spectrometer HPGe with a germanium semiconductor detector type REGe (brand CAMBERRA, model GR6022) (Table 1). Gamma measurements were also carried out at sample locations using a NaI scintillation probe. Gamma contribution derived from in situ measurements was compared to that derived from high-resolution gamma spectrometry finding no significant differences. High-resolution gamma spectrometry was preferred over in situ measurements as it allows storing the samples in tight containers and left to reach secular equilibrium before measurement. A linear accumulation of sediments has been assumed in order to calculate the contribution of cosmic radiation according to varying burial depth (Prescott and Hutton 1994). Attenuation caused by moisture and grain size (Bell 1979; Guerin et al. 2012) was taken into account. An uncertainty of 5% has been added to water contents to account for variability during the burial period. Total dose rates were calculated using

the dose rate and age calculator (DRAC, Durcan et al. 2015) and are summarized in Table 1.

Additionally, six samples had been previously collected (field campaigns in 2010, 2012 and 2014) at PA and A23H outcrops, then processed by Laboratorio de Datación y Radioquímica de la Universidad Autónoma de Madrid. These samples were measured over the polymineral fine grain (2–10 µm) fraction. Anomalous fading tests indicated that fading of the OSL signal was not significant for these samples. Annual dose rates were derived from the contribution of K-40, measured with a Geiger–Müller system, and the contribution of uranium and thorium measured with a ZnS solid scintillator. Uncertainties associated with the calculated annual dose rates for these samples were not reported, but considered for age estimation.

## Structure and morphotectonics of the Calamocha fault

### Structural description

The northern sector of the Calamocha normal fault zone brings into contact Palaeozoic and middle Miocene rocks, at the footwall block, with Late Neogene units (R2, P2 and R3), at the hanging-wall block (Figs. 3 and 4a). A reverse fault, inherited from the Early Miocene contractional structuration of the Calatayud basin, is kept between the normal faults. The fault trace trends N140° E and veers to N120° E close to its northern tip, where the fault surface is clearly exposed (Fig. 5a, c). At the Venta de los Céntimos

**Table 1** Summary of the parameters and derived ages of samples dated with OSL from the ZSR trench (at the Luminescence Dating Laboratory of CENIEH, Burgos, Spain), and from the PA and A23H slopes (at the Laboratorio de Datación y Radioquímica de la Universidad Autónoma, Madrid, Spain)

Sample	Trench location	Depth (m)	Dose rate (Gy/ka)	Equivalent dose (Gy)	Age (ka)
CALT-3B	ZSR	2.5	1.93 ± 0.07	236.7 ± 9.9	122.6 ± 7.0
CALT-3Bb	ZSR	1.7	3.35 ± 0.14	295.3 ± 10.1	88.2 ± 4.9
CALT-4D	ZSR	0.5	2.88 ± 0.10	294.5 ± 13.4	102.2 ± 5.9
CALT-5B	ZSR	2.0	2.10 ± 0.10	144.5 ± 8.7	68.9 ± 5.2
CALT-7D	ZSR	0.5	2.32 ± 0.08	171.6 ± 10.0	73.8 ± 5.0
CALT-7A	ZSR	3.0	2.26 ± 0.07	329.1 ± 17.4	145.9 ± 9.1
CALT-8B	ZSR	2.3	1.57 ± 0.06	210.2 ± 13.8	134.0 ± 10.3
CALT-8Bb	ZSR	2.1	1.62 ± 0.07	205.5 ± 8.8	126.7 ± 7.6
CALT-5Ua	ZSR	1.7	1.84 ± 0.08	265.0 ± 11.1	144.1 ± 8.5
CALT-8C	ZSR	1.3	2.14 ± 0.08	233.0 ± 16.6	108.9 ± 8.8
MAD-5764SDA	PA	0.8	3.6	253.80	69.9 ± 5.5
MAD-6334BIN	PA	10.0	1.8	168.86	95.4 ± 6.3
MAD-6332BIN	A23H	0.5	4.8	66.26	13.8 ± 0.9
MAD-6165rBIN	A23H	1.7	3.4	119.00	35.3 ± 0.9
MAD-6177rBIN	A23H	3.0	2.1	114.26	53.1 ± 3.7
MAD-6180rBIN	A23H	2.0	3.6	150.85	41.9 ± 2.9

Uncertainties associated with the estimated dose rates and equivalent doses from PA and A23H slopes were not reported. All ages are reported at 1-sigma ( $k = 1$ )

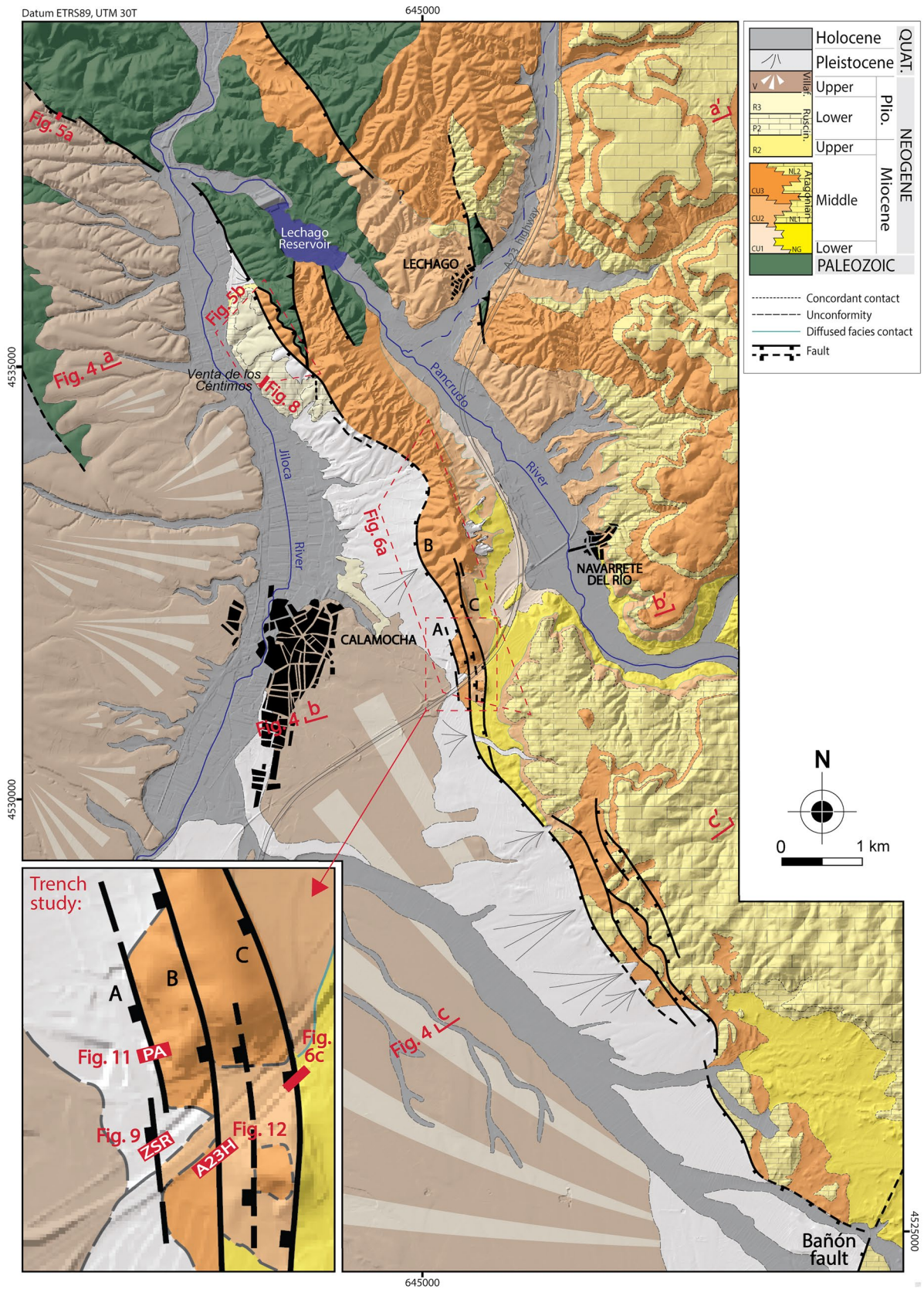




**Fig. 3** Geological map of the Calamocha area (on DEM image from IGN) showing the main structures associated with the Calamocha fault (modified from Martín-Bello et al. 2014). Location of Figs. 6a, b, 7a, c, 9, 10, 12 and 13, and cross sections of Fig. 5a, b, c, are indicated. The inset shows the location of trenches: Zaragoza–Sagunto Railway (ZSR), Polígono Agroalimentario (PA), and A-23 highway (A23H)

area (Fig. 3), the main fault does not crop out, but the abrupt contact between slightly tilted P2 limestones and Palaeozoic materials can be recognized (Fig. 5b). Numerous minor fractures, mostly striking NNW–SSE, have been observed close to the fault within unit R3 (Fig. 5d). To the south, the fault trace becomes more sinuous, and brings into contact Miocene clastic materials (CU3) with Pleistocene alluvial fans that spread from the fault scarp.

In the central sector, the Calamocha fault splits into several, nearly parallel synthetic branches (faults A, B, C in Figs. 3, 4b and 6a). Two of them (faults B and C) crop out in the A-23 highway slopes and bring into contact different Miocene clastic units (NL2, CU2 and CU3; Fig. 6b, c). In particular, fault branch B, locally oriented N178° E, 75° W, can be clearly observed on a slope adjacent to the highway; at its hanging-wall block, the CU3 unit, made of quartzitic pebbles with interbedded red siltstones, strongly dips to the west suggesting the occurrence of a sharp normal drag fold. Unit CU3 finally lies in contact with the Pleistocene alluvial deposits through the westernmost fault (A), with average orientation N160° E, 70° W. The ca. 1-km-long trace of this fault branch can be recognized both in the field and orthoimages, and was excellently exposed for several years in an artificial slope at the Polígono Agroalimentario (agri-food industrial estate) of Calamocha.

At its southern sector, the Calamocha fault brings into contact Miocene units with Pleistocene alluvial fans that partially cover the Villafranchian pediment (Fig. 4c). The footwall block is affected by a monocline whose shortest limb dips up to 17° SW and is offset by two antithetic faults that duplicate the CU3–NL2 sequence in surface. At the SSE tip of the Calamocha fault, it abuts the transverse Bañón fault (Fig. 3).

### Fault kinematics

Kinematic data of the Calamocha fault are only available from its central sector. As reported below (“[The Calamocha fault and associated deformation within the regional framework](#)” and “[Seismogenic characterization](#)”), slickenlines observed on fault branches A and B show prevailing transport directions (azimuth of the slip vector on the hanging-wall block) towards W and SW, representing slip vectors with rake mostly constrained between 85° N and 75° S on the local fault surfaces, i.e., nearly pure normal slip.

Calculating the fault throw is not an easy task, owing to the lack of unambiguous stratigraphic markers recognizable at both fault walls. Rubio and Simón (2007) estimated a minimum vertical throw of 160–180 m in the northern segment based on a hypothetical contemporaneity of units R2 and/or P2 of the hanging-wall block with a clastic unit that crops out to the east of Lechago village (unit 38 of Hernández et al. 1983; lower Pliocene).

At present, a better approach is feasible thanks to geomorphological markers, i.e., the planation surfaces described in “[Morphotectonic evolution: late neogene planation surfaces](#)”. The morphotectonic map of Fig. 7 shows the remains of such surfaces in the area surrounding the Calamocha fault, together with the contours of FES2 and FES3, and recent faults that offset them. FES3 is the most useful marker since it is present in both fault blocks. East of Calamocha, it constitutes a widespread erosion level modelling the Miocene materials of the footwall block, at heights that decrease northwards from ca. 1150 to 1040 m a.s.l. North of Calamocha, it is exposed within the hanging-wall block at the Venta de los Céntimos area, represented by its correlative sedimentary level, i.e., the stratigraphic limit between units P2 and R3, at about 880–900 m a.s.l. Such a morpho-sedimentary setting is analogous to that widely described in the Teruel basin (e.g., Ezquerro et al. 2020). Further north-east, at the hanging-wall block of the Cucalón–Pancrudo fault, erosional FES3 is also overlaid by the R3 unit, the latter being 60–80 m thick and modelled by a Villafranchian pediment. In this case, FES3 is expressed as the stratigraphic boundary between middle Miocene carbonates and R3 alluvial clastics, its height being constrained from map information.

The throw recorded by FES3 in the northern sector of the Calamocha fault is calculated to 150–180 m, similar to that estimated by Rubio and Simón (2007) based on less precise morpho-sedimentary correlation. According to the contours of Fig. 7, the throw accommodated at the central sector approaches 130–150 m, while it decreases to about 100 m in the southern one.

Assuming the basic geometric and kinematical parameters formerly referred (fault dip: 70–75° W; slip vector rake: 85° N to 75° S), as well as the aforementioned maximum throw (150–180 m), the maximum post-FES3 net slip in the northern and central sectors of the Calamocha fault can be estimated in the range of 155–195 m. Considering the age of the FES3 planation surface (3.5 Ma; “[Morphotectonic evolution: late neogene planation surfaces](#)”), this results in a slip rate of 0.045–0.055 mm/a.

Although FES3 constitutes the most valuable marker for calculating the long-term slip and slip rate, this does not mean that the entire history of the fault started after that planation event. The possibility of earlier movements has been directly explored at the only area where materials slightly older than FES3 crop out close to the fault (P2 unit in Venta

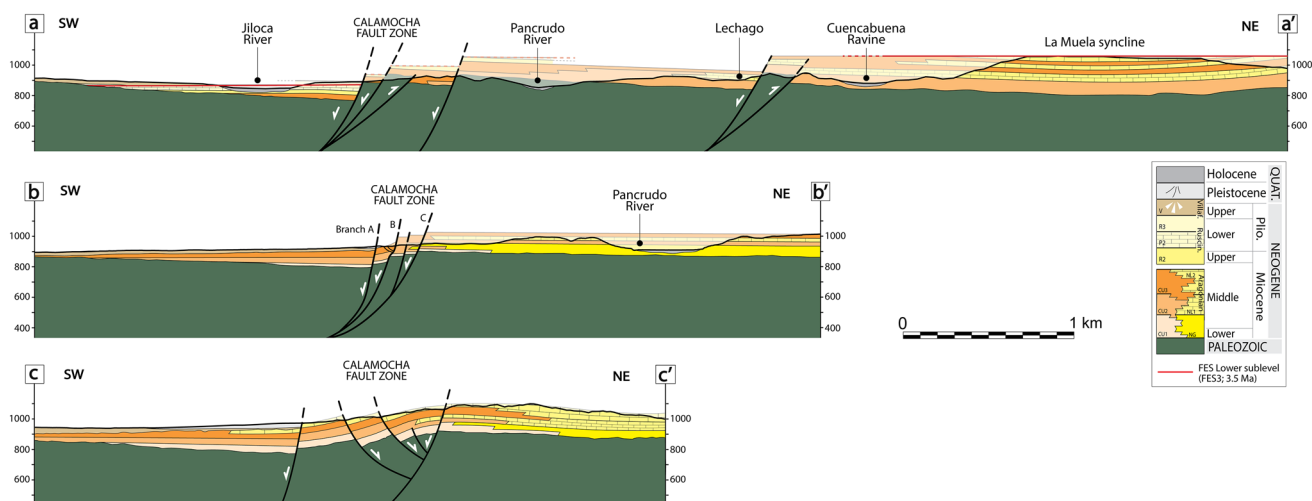


**Fig. 4** Cross sections of the Calamocha fault at its northern **a**, central (**b**; modified from Martín-Bello et al. 2014) and southern sectors **c**. See location in Fig. 4

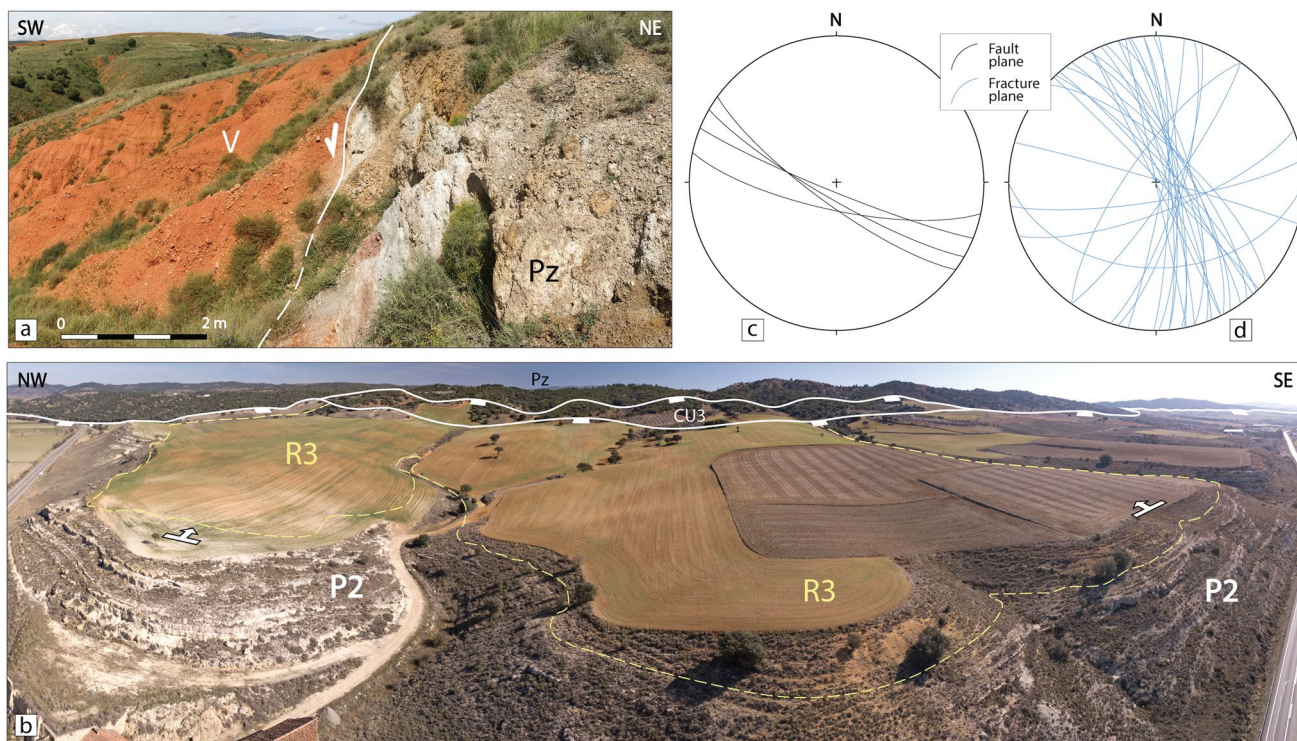


**Fig. 5 a** Exposure of the Calamocha fault close to its northern tip, separating Villafranchian red clastics (V) from Palaeozoic (Pz). **b** Oblique aerial view of Venta de los Céntimos area (VC in Fig. 4), showing the fault scarp separating the slightly tilted (about 5° towards E) limestones of P2 unit and red clastics of R3 unit from CU3 and

Palaeozoic. **c** Stereoplot (equal area, lower hemisphere) depicting orientations of fault surfaces measured in outcrop a. **d** Stereoplot (equal area, lower hemisphere) depicting orientations of fractures measured in R3 unit. See location in Fig. 4

de los Céntimos area). Limestone and marl beds of P2 in the hanging-wall block show metre- to decametre-scale normal faults with associated changes in the thickness of certain stratigraphic levels (Fig. 8a), therefore being interpreted

as coeval with sedimentation. These syndimentary faults have NNW–SSE strike and east dip, i.e., they are synthetic to the Calamocha fault and nearly parallel to fractures measured in the R3 unit (Fig. 5d). A few metres apart, the same





**Fig. 6** **a** Oblique aerial view of the area east of Calamocha town, where the traces of fault branches A, B and C representing the central sector of the Calamocha fault zone are drawn. **b** Branch B exposed

at a service road adjacent to A-23 highway. **c** Branch C exposed at the A-23 slope. Location of the slopes ZSR, PA and A23H, and their respective Figs. 10, 12 and 13, are indicated

deformed beds also show gentle, upright folds with local thickening and thinning, interpreted as soft-sediment deformation structures.

Such tectono-sedimentary setting suggests that: (i) the negative inversion of the Calamocha fault would have initiated prior to development of FES3 surface, at least coeval with the deposition of the P2 unit (so probably coeval with onset of the Conclud fault, close to the age of FES2, ca. 3.8 Ma; Ezquerro et al. 2020); (ii) the total accumulated displacement on the fault could be slightly higher than that formerly established, increased by a value equivalent to a fraction of the thickness of unit P2 (up to a 30 m). In such a scenario, the maximum throw at the Calamocha fault is in the range of 180–210 m, and the maximum net slip in the range of 190–230 m. The estimate of average long-term slip rate (3.8 Ma) does not change significantly: 0.05–0.06 mm/a.

### Trench study

The target of our palaeoseismological study has been the western branches of the Calamocha fault (A and B), east of Calamocha town. Three artificial slopes, trending nearly orthogonal to the fault traces and dipping about 45–50° have been the object of detailed study (see location in Figs. 3 and 6a): Zaragoza–Sagunto railway (ZSR), Polígono Agroalimentario (PA), and A-23 highway

(A23H). The ZSR site constitutes the main source of palaeoseismological information, while PA and A23H have provided complementary data about structures whose ages are less constrained.

### Zaragoza–Sagunto Railway (ZSR)

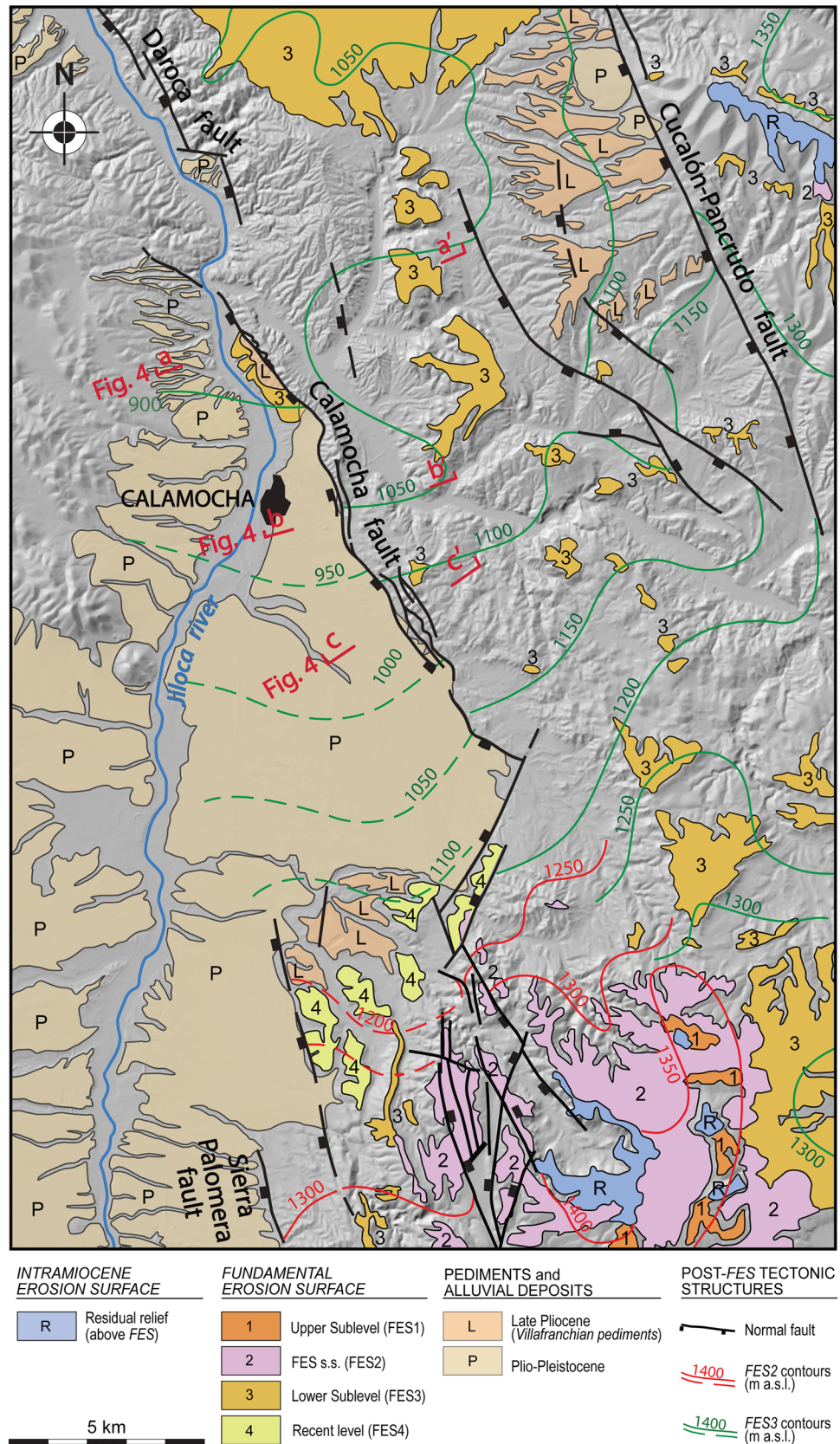
A segment of artificial slope of the Zaragoza–Sagunto railway was surveyed, representing an N055° E trending, 45-m-long trench that exposes branch A (ZSR; Fig. 9; see location in Figs. 3 and 6A).

### Materials

Materials cropping out in the trench are alluvial Pleistocene sediments unconformably lying on Neogene greyish mudstone with interbedded grey limestone and ochre sand, all of them in decimetre-scale tabular strata dipping to the SW. Seven Pleistocene units have been distinguished on the basis of their lithology (Fig. 9a, b):

- Unit 1 (50 cm thick, in average) is made of orange mudstone with white carbonate nodules up to 25 cm in diameter, the latter disappearing towards the uppermost sandy part of the unit. This unit is only present within the western block.

**Fig. 7** Morphotectonic map of the study area, showing remains of late Neogene planation surfaces, their height contours and recent faults. See location in Fig. 1b





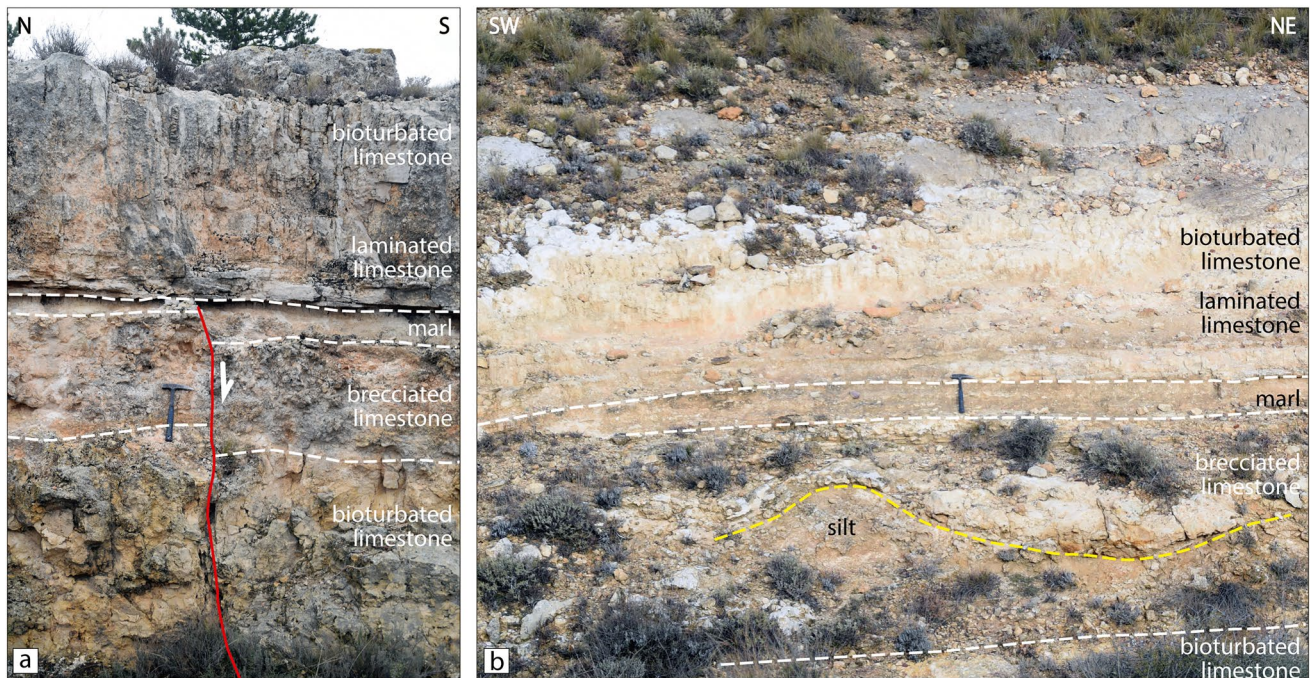


**Fig. 8** Syndimentary structures in P2 unit at the Venta de los Céntimos area. **a** Normal fault exhibiting differential displacement in successive beds. **b** Soft-sediment deformation structures (SSDS, gentle folds). See location in Fig. 4

- Unit 2 (35–75 cm) corresponds to a fining-upwards irregular bed with erosional base, made of whitish, grain-supported pebble gravel with brownish sandy matrix. Clasts of quartzite and limestone are mainly subangular to subrounded in shape. Some rip-up mud clasts were also identified.
- Unit 3 (25 cm) consists of whitish, grain-supported gravel with angular to subangular, mm- to dm-scale clasts, making up a tabular, calcrete-topped, fining-upwards cycle. This unit is only present within the western block.
- Unit 4 (40 cm) is made up of reddish, grain-supported gravel with angular to subangular mm- to dm-scale clasts arranged in a fining-upwards cycle. This unit is only present within the western block.
- Unit 5 (140 cm) consists of brown, pedogenized mudstone with carbonate nodules up to 25 cm in size, dispersed angular–subangular clasts, and rare interbedded grey sand levels. Carbonate nodules are less common towards the base and the top of the unit. This unit is only present within the eastern block.
- Unit 6 (110 cm) is formed by light orange, disorganized gravel with subangular clasts (up 25 cm in size) and white carbonate nodules.
- Unit 7 (until 140 cm) is made up of grain-supported gravel, orange in colour, with channel geometry. This unit is only present within the western block.
- Unit 8 is a nearly vertical structureless body of orange silt with scarce floating, angular to subangular limestone clasts.
- Unit 9 (20 cm) corresponds to a surficial regolith made up of reddish sandy mudstone with disperse granules.

#### OSL dating

The OSL response from the ten samples measured is fast-component dominated, and their reliability to estimate the accumulated dose has been confirmed through dose recovery tests performed in the laboratory. The derived natural dose populations are normally distributed with overdispersion values below 30% after removing outliers. Estimated burial equivalent doses, total dose rates and derived numerical ages are summarized in Table 1. Sample CALT-3Bb showed an anomalously large dose rate compared to the rest of the samples from this trench. This led to too young an age, disagreeing with the sedimentary succession. This age has therefore been discarded from the study and from any further discussion. Ages finally adopted are labelled in Fig. 9b.

#### Structural description

An extensional fault zone, with faults that are both synthetic and antithetic to the Calamocha fault system, is exposed



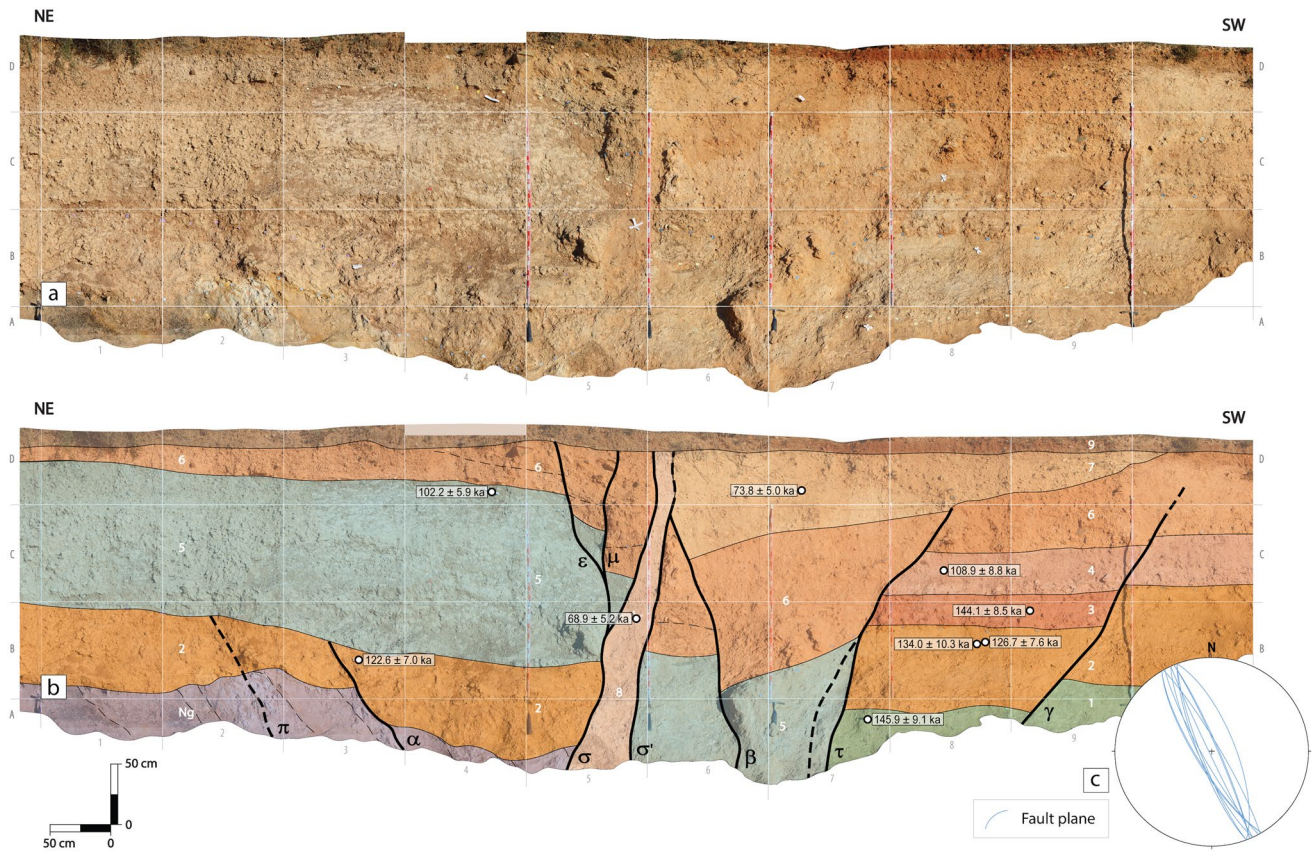


**Fig. 9** **a** Photomosaic of the ZSR trench that crosses branch A; see location in Figs. 4 and 7a. **b** Detailed log. 1–9: Quaternary units described in the text. Greek characters: faults referred in the text. The

location and age of samples dated by OSL is indicated. **c** Stereoplots (equal area, lower hemisphere) showing orientations of fault planes measured within the trench

within the ZSR log (Fig. 9b). It cuts the trench wall obliquely and can be identified with the southern prolongation of synthetic branch A (Fig. 3), although antithetic faults are also exposed. The stereoplots of Fig. 9c shows the homogeneous NNW–SSE strike and ca. 80° dip of every fault plane measured along the trench. No kinematic indicator has been observed on them.

Faults at both the eastern and central sectors are synthetic with the Calamocha fault (Fig. 9b). The eastern sector of the trench is cut by fault  $\alpha$  (accompanied by fracture  $\pi$ ), which underwent vertical displacement (throw)  $\approx 0.3$  m after sedimentation of unit 2 and is covered by unit 5. Faults  $\varepsilon$ ,  $\mu$ ,  $\sigma$ ,  $\sigma'$  and  $\beta$  make up the central fault zone, with an associated open fissure bounded by surfaces  $\sigma$  and  $\sigma'$  and filled with unit 8. Surfaces  $\sigma$  and  $\sigma'$  are irregular and show high apparent projected dips that mainly respond to the oblique orientation of the structure with respect to the trench direction, and the subsequent projection of the slope onto the vertical plane. Faults  $\varepsilon$  and  $\mu$  are associated with  $\sigma$  as two splay faults, jointly producing a throw of more than 0.7 m in the contact between units 5 and 6. The rock body enclosed by surfaces  $\sigma$  and  $\sigma'$  (unit 8) is interpreted as a fissure infill based on its

nearly vertical, transverse attitude and its massive, disorganized internal constitution. According to this interpretation, such surfaces would have represented both walls of a single fracture, then they were disengaged and partially crumbled before infilling took place. Fault propagated through units 5, 6 and 7 producing a localized rollover structure.

Faults exposed at the western sector,  $\gamma$  and  $\tau$ , are antithetic to the Calamocha fault (Fig. 9b). Fault  $\gamma$  offsets  $\approx 0.4$  m the base of unit 2, while producing a smaller separation (ca. 0.1 m) in the base of unit 4. We have interpreted that it underwent displacement  $\approx 0.3$  m before sedimentation of unit 2, and was then reactivated after the deposition of unit 6. Fault  $\tau$  played an important role producing the highest antithetic displacement and allowing syntectonic deposit of unit 5 (as it is only visible in its hanging-wall block). It also offsets unit 6, so it has undergone reactivation after the deposition of this unit and has been covered by unit 7, in the same way as fault  $\gamma$ .

After deposition of unit 2, the aggregate, visible throw of the synthetic faults ( $\approx 2$  m) is virtually counterbalanced by the antithetic throw, as can be seen by comparing the height of the base of unit 2 at both ends of the log (Fig. 9b). In

**Fig. 10** Evolutionary model of sedimentation and deformation recorded at the ZSR trench from retrodeformational analysis. Each sketch represents a stage subsequent to the palaeoseismic event (and, in some cases, to deposition of sedimentary units) labelled above. Unexposed sectors below the trench have been locally reconstructed in the sketches to complete the evolutionary model. Bold traces represent faults active during each event

addition, a supposed synthetic offset of unit 1 (with throw equal of greater than its own thickness), previous to deposition of unit 2, could justify the absence of the former in the western block and the deeper position of the Neogene/Pleistocene boundary in the eastern one.

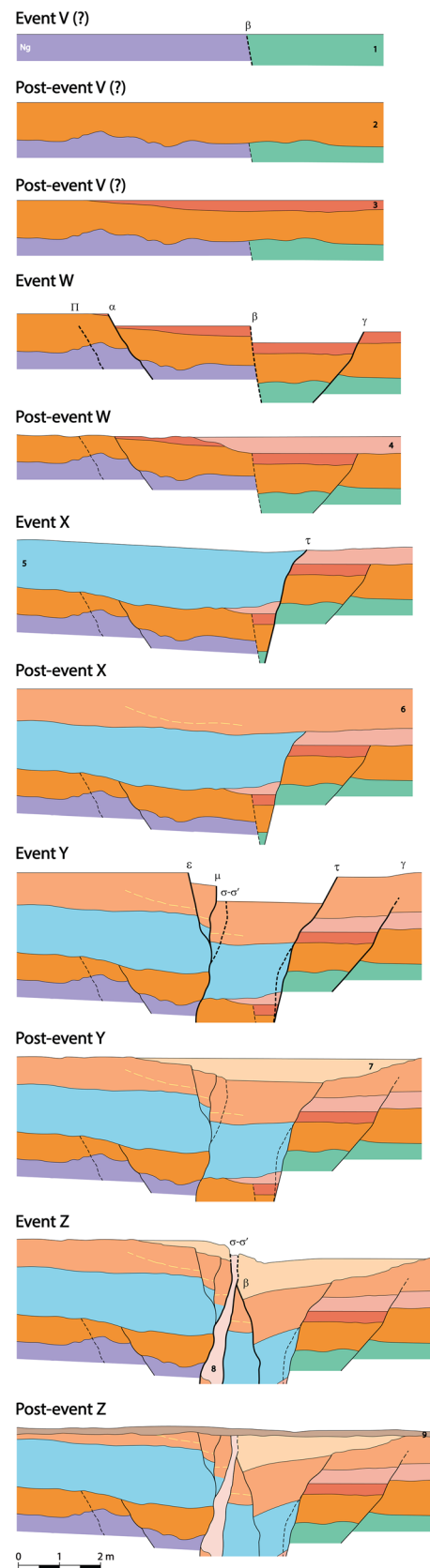
As explained above, throw values cannot be translated into net slip due to the lack of information about slip vectors on the surveyed faults. In addition, doubts about the kinematical meaning of antithetic faults and weak chronological constrains also prevent a reliable approach to slip rates.

### Interpretation of palaeoseismic events and retrodeformational analysis

Detailed study of sedimentary units, deformation and relationship with faults allows interpreting four clear deformation events (W to Z), and an additional uncertain one (V), at the ZSR. As an auxiliary tool, retrodeformational analysis of the trench log (Fig. 10) was achieved to contrast the succession of deformation events and to test its kinematic consistence. Several identifiable faults were either formed, propagated or reactivated during each deformation event. For each event, fault throws were computed, while progressive horizontal extension is visually expressed in the successive cross sections of Fig. 10.

The interpreted events at the ZSR are as follows (see Figs. 10b and 11):

- Event V (?) is tentatively inferred from the absence of unit 1 above the Neogene in the eastern block, which can be reliably explained by slip on fault  $\beta$  after deposition of unit 1 and prior to unit 2. A second scenario, i.e., an erosional unconformity between both units, cannot be ruled out. Event V would be pre-dated by the top of unit 1 ( $145.9 \pm 9.1$  ka) and post-dated by unit 2 (with a range age of  $144.3$ – $135.6$  ka, result of the overlap of  $122.6 \pm 7.0$ ,  $126.7 \pm 7.6$ ,  $134.0 \pm 10.3$  and  $144.1 \pm 8.5$  ka). The more probable event age would be adopted as ca. 140 ka. The throw associated with this hypothetical event should be equal to or greater than the exposed thickness of unit 1 ( $\approx 0.5$  m).
- Event W is initially identified from rupture and displacement of units 2 and 3 by the antithetic fault  $\gamma$ , prior to deposition of unit 4. This explains why the offset in unit 2 is greater than that in unit 4, and why unit 3 is only present in its hanging-wall block. Hypotheti-





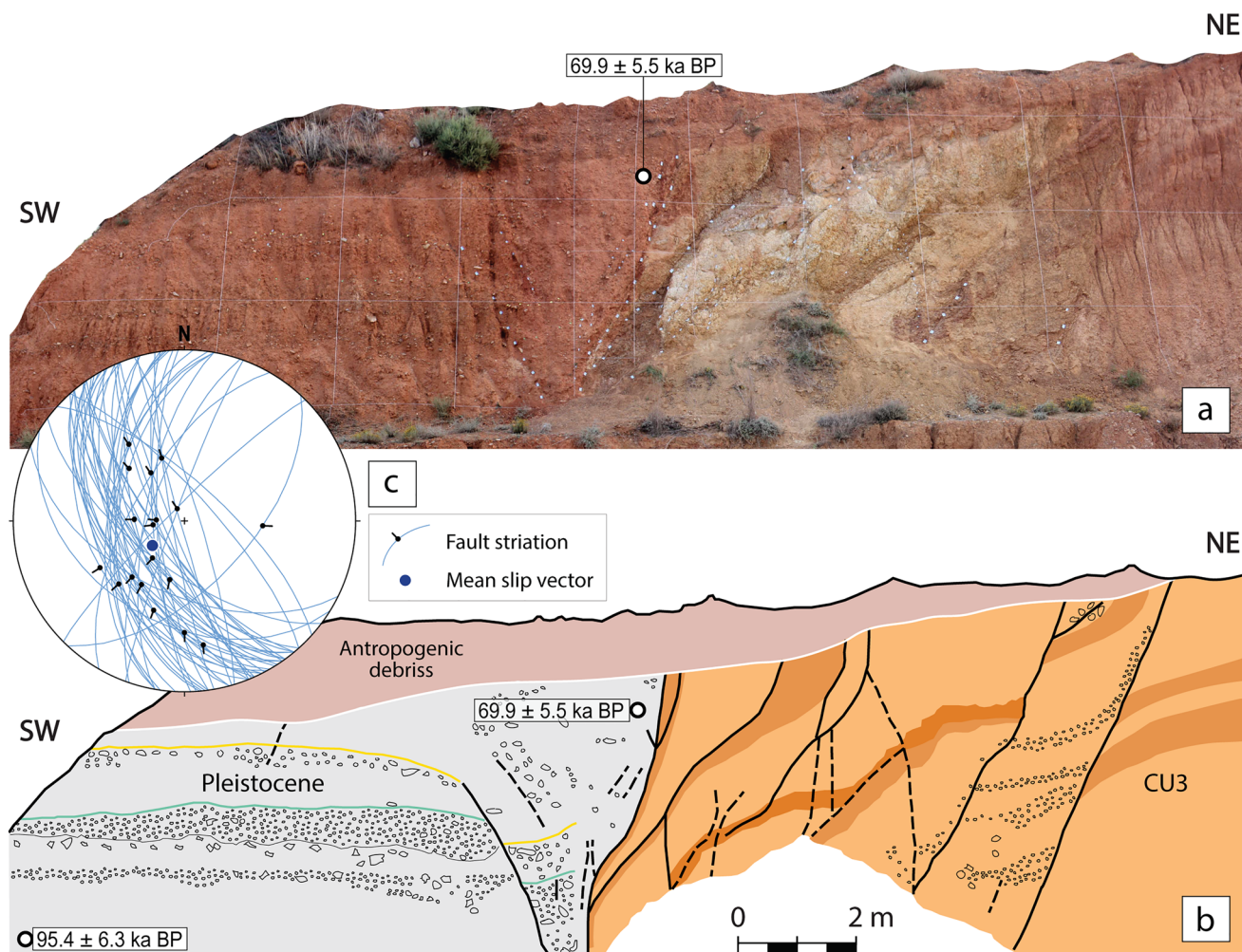


**Fig. 11** **a** Photomosaic of the PA slope that crosses branch A; see location in Figs. 4 and 7a. **b** Synthetic log showing the Miocene Clastic Unit 3 (CU3) and Pleistocene deposits (modified from Martín

Bello et al. 2014). The location and age of samples dated by OSL are indicated. **c** Stereoplot (equal area, lower hemisphere) showing orientations of fault planes and slickenlines measured within the outcrop

- cal simultaneous slip on fault  $\beta$  could justify the loss of unit 3 in the eastern block. Faults  $\alpha$  and  $\pi$ , overlaid by unit 5, have been also attributed to this event on the basis of the principle of parsimony (in order to minimize the number of events necessary for explaining the observed structures). This event is pre-dated by unit 2 (in the range of 144.3–135.6 ka) and post-dated by unit 4 ( $108.9 \pm 8.8$  ka). The more probable event age would be closer to the first range, and adopted as ca. 125 ka. Synthetic and antithetic slip has been counterbalanced in this event, resulting in a total synthetic throw of  $\approx 0.45$  m and a horizontal extension of  $\approx 0.45$  m.
- Event X is interpreted from the existence of unit 5 only within the eastern block due to syn/post-sedimentary displacement by fault  $\tau$ . It should be pre-dated by unit 4 ( $108.9 \pm 8.8$  ka) and post-dated by the top of unit 5 ( $102.2 \pm 5.9$  ka). The more probable event age would be

adopted as ca. 105 ka. The total, antithetic throw of this event is  $\approx 1.1$  m and its horizontal extension  $\approx 0.3$  m.

- Event Y is identified from rupture and displacement of unit 6 by faults  $\varepsilon$ ,  $\mu$ ,  $\sigma$ ,  $\sigma'$ ,  $\tau$  and  $\gamma$ . It is pre-dated by unit 5 ( $102.2 \pm 5.9$  ka) and post-dated by unit 7 ( $73.8 \pm 5.0$  ka). The more probable event age would be closer to the second age and adopted as ca. 80 ka. The total throw of this event is virtually null due to counterbalancing of synthetic and antithetic slip, and its horizontal extension  $\approx 0.2$  m.
- Event Z is interpreted from the displacement and rollover tilting of unit 7 by fault  $\beta$  and from the disengagement of surfaces  $\sigma$  and  $\sigma'$  that results in fissure opening and infill with unit 8. It is pre-dated by unit 7 ( $73.8 \pm 5.0$  ka) and post-dated by unit 8 ( $68.9 \pm 5.2$  ka). The more probable event age adopted is ca. 70 ka. The total synthetic throw



of this event is  $\approx 0.5$  m and its horizontal extension  $\approx 0.25$  m.

### Polígono agroalimentario (PA)

PA site was an N075° E trending, 20-m-long artificial slope at the margin of the Calamocha agri-food industrial estate, which also intersected fault branch A. It was removed during recent widening of the industrial area, but it had already been analysed and fully documented before.

The trace of fault branch A, bringing into contact Pleistocene sediments within the hanging-wall and unit CU3 within the footwall, was recognized in this outcrop (Fig. 11a, b). Quaternary sediments are significantly homogeneous, so that no well-defined unit could be distinguished at that formerly existing slope. Pleistocene alluvial sediments consist of gravel with quartzitic clasts and red lutite matrix. Some clasts are aligned defining subtle levels that can be locally recognized. Lithology of unit CU3 mainly consists of marl and limestone, bedding being strongly disrupted due to both brittle and ductile deformation.

The chronology of the involved Pleistocene sediments has been constrained from two OSL ages. These were provided by two samples collected, respectively, at the base of the visible Pleistocene succession ( $95.4 \pm 6.3$  ka) and within the youngest sediments cut by the fault ( $69.9 \pm 5.5$  ka) (see Table 1). The overlying materials are present-day debris of anthropogenic origin.

The main fault surface has an average orientation N160° E, 70° W. Subsidiary rupture surfaces exposed at the slope mainly affected the footwall block and were synthetic with the main fault A, striking NNW–SSE and dipping between 45° and 80° W (Fig. 11c). There were some antithetic faults propagated through the hanging-wall block, one of them with a throw of ca. 1.1 m. The slickenlines measured within the fault zone indicate a prevailing normal slip, with most slip vectors towards W and SW (mean transport direction towards N234° E; Fig. 11c).

The described features suggest that fault A was active as a nearly pure normal fault during the Late Pleistocene, probably during deposition of the alluvial sediments occupying the hanging-wall block ( $95.4 \pm 6.3$  to  $69.9 \pm 5.5$  ka, approximately), and definitely after them. The minimum fault throw accumulated during that time span can be approached from: (i) the sedimentary thickness between both dated samples (ca. 4.5 m), assuming that slip rate and sedimentation rate are similar to each other; (ii) the difference between the visible throw at the main fault minus the throw accommodated by the antithetic fault:  $(4.8 - 1.1) \text{ m} = 3.7$  m. Considering the average fault dip (70°) and assuming the slip direction previously inferred (N234° E), the resulting net slip would be in the range of 3.9–4.8 m, and the slip rate could be roughly estimated to 0.1–0.3 mm/a.

### A-23 highway slope (A23H)

A23H site is a N055° E trending, 110-m-long slope segment of the service road adjacent to the A-23 highway. It exposes fault branch B, which brings into contact two middle Miocene units: siltstone and claystone of CU2, within the footwall block, and gravel of subrounded clasts CU3, within the hanging-wall block (Figs. 6b, 12a). Bedding of the unit CU2 is difficult to identify owing to intense bending and brecciation, while conspicuous alignments of quartzitic pebbles and carbonated crusts define bedding within CU3. The main fault plane ( $\delta$  in Fig. 12b) is locally oriented N178° E, 75° W, with slickenlines indicating a slip vector towards N270° E (Fig. 12d).

The footwall block is affected by minor synthetic faults and fractures, which strike close to N–S and dip between 50° and 80° W (Fig. 12d). Within the hanging-wall block a high number of antithetic faults can be recognized, also striking around N–S and dipping 30–50° E. They produce apparent displacements of 0.5–3 m in the pebble alignments that define the bedding, the latter dipping 25°–45° W (see close view in Fig. 12c).

Such fault association suggests a rollover structure induced by listric geometry of the main fault. Passive accommodation of the hanging-wall deformation would have occurred through a mechanism of antithetic simple shear achieved by slip over discrete planes. However, bedding does not dip towards the main fault, but synthetic with it (up to a maximum of 45° SW in an inflection zone at 60 m to the fault). The bedding attitude suggests the occurrence of additional normal drag folding. The reduced dip of the antithetic faults and, on the contrary, the wide angle between these faults and bedding indicates that these faults were formed prior to the drag fold, and then reduced their dips while bedding was tilted. We interpret that such deformation sequence could be achieved by slip of the hanging-wall block on an undulated rupture surface made of a shallow listric segment, then on an increasingly dipping deep segment.

Some of the antithetic faults (mainly those propagating further down into the hanging-wall block) are overlaid by two colluvial bodies (Q1 and Q2 in Fig. 12a) with erosive base. Both are made of gravel (angular limestone pebbles) with interbedded medium-fine sand, and are dated to  $41.9 \pm 2.9$  and  $53.1 \pm 3.7$  ka, respectively (see Table 1).

Two other colluvial bodies (Q3 and Q4) are affected by faults (Fig. 12a, b):

- Colluvium Q3 is made of grain-supported gravel (angular limestone pebbles up to 20 cm in diameter). The sedimentary body is channel-shaped, shows subhorizontal layering marked by interbedded fine sand levels, and is dated to  $35.3 \pm 2.3$  ka. It also overlies two of the antithetic faults, but another one ( $\rho$ ) in the hanging-wall

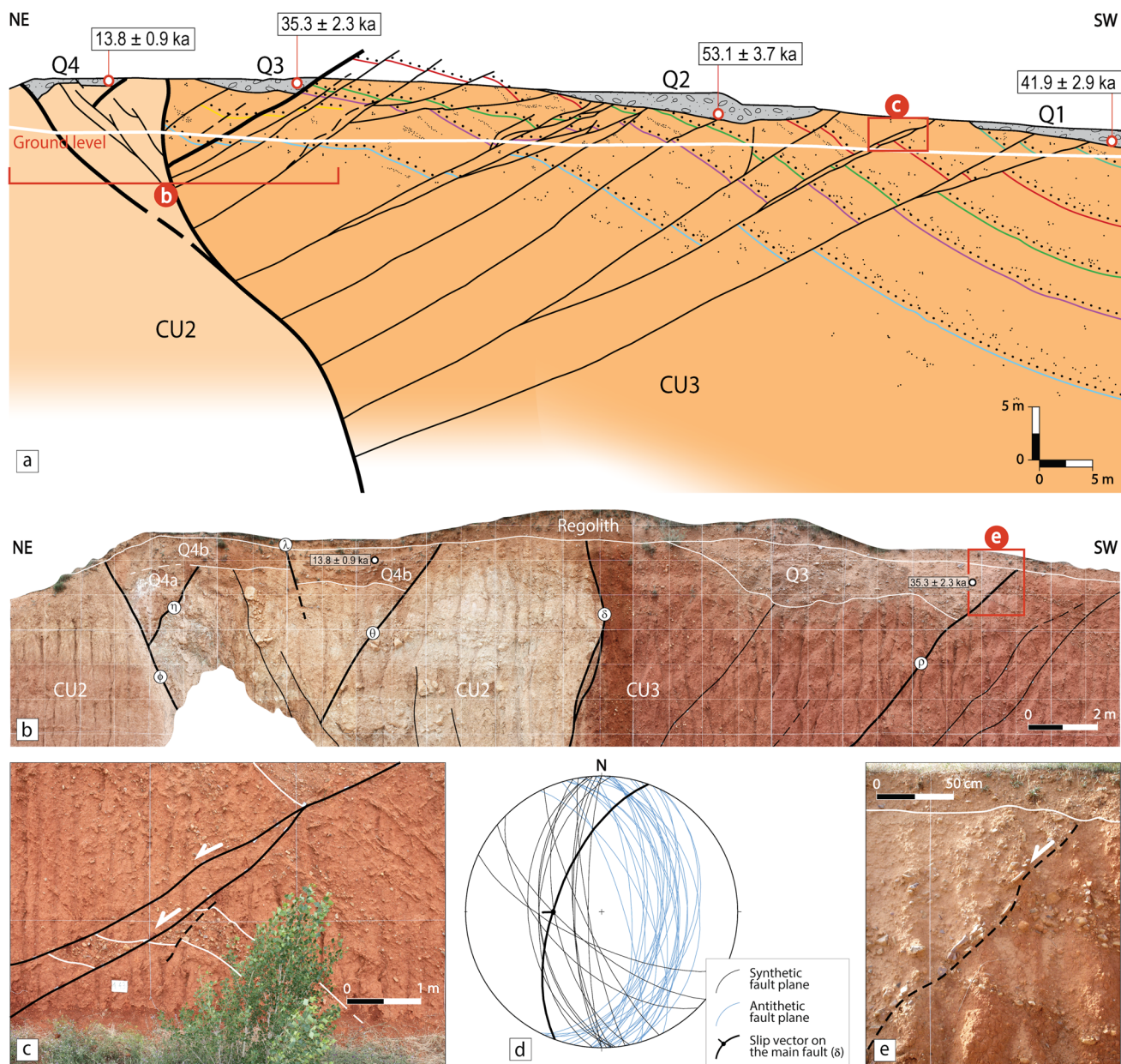


**Fig. 12** **a** Synthetic cross section (aboveground) of the A23H slope that crosses branch B, and its interpretation (belowground). Bedding of the Miocene clastic unit CU3 in the hanging-wall block can be recognized by conspicuous quartzitic gravel horizons, unconformably underlying Quaternary colluviums Q1–Q4. The position and age of samples dated by OSL is indicated. See location in Figs. 4 and 7a. Modified from Martín-Bello et al. (2014). **b** Interpreted photomosaic

of deformed colluvium bodies Q3 and Q4. Sections a and b are drawn from photomosaics of the artificial slope projected onto the vertical plane. **c** Details of bedding of unit CU3 cut by antithetic faults. **d** Stereoplot (equal area, lower hemisphere) showing orientations of synthetic and antithetic faults, as well as striation on the main fault plane ( $\delta$ ). **e** Details of aligned pebbles of Q3 along the fault ( $\rho$ )

block, striking N005° E and dipping 64° E, cuts the deposit and produces reorientation of pebbles (Fig. 12e), with a minimum throw of 1.5 m. Assuming a slip vector towards N090° E (within the same movement plane of fault  $\delta$ ; i.e., nearly pure normal movement), this involves a net slip of ~1.7 m (Fig. 12b).

– Colluvium Q4 is a massive and nearly tabular body of fine sand with two interbedded levels of matrix-supported gravel (angular-subangular limestone pebbles up to 15 cm in diameter). It has delivered an OSL age  $13.8 \pm 0.9$  ka. The sedimentary body overlies the main fault zone, and is delimited by two main mechanical

boundaries which correspond to a synthetic fault ( $\phi$ ), oriented 175, 52 W, and an antithetic one ( $\theta$ ), oriented 174, 60 E. They produce throws of 2,4 m and 1,3 m, respectively, which would correspond to net slips  $\sim 3.0$  m and  $\sim 1.4$  m. Another two faults ( $\eta$  and  $\lambda$ ) also cut the base of Q4, showing net slip of  $\sim 1.6$  m and  $\sim 0.4$ , respectively (Fig. 12b). Very probably, the displacement recorded at fault  $\phi$  does not represent a single event. Fault  $\eta$  cuts subunit Q4a and is overlaid by the base of Q4b, which in turn is offset by faults  $\phi$ ,  $\lambda$  and  $\theta$ . At least two faulting episodes are therefore required for explaining the deformation of Q4.

According to the proposed kinematic model, recent reactivation of antithetic faults should have been induced by slip events on fault branch B. Overall, activation of subsidiary rupture surfaces would have developed progressively closer to the main fault. It all corroborates that the Calamocha fault has undergone recurrent slip events during the Late Pleistocene: some of them prior to  $53.1 \pm 3.7$ ,  $41.9 \pm 2.9$  and  $35.3 \pm 2.3$  ka, others after  $35.3 \pm 2.3$  ka and  $13.8 \pm 0.9$ , respectively.

## Discussion

### Assessing long-term and short-term activity of the Calamocha fault and its palaeoseismic significance

The geometry, kinematics and evolution of the Calamocha fault have been characterized from structural and morphotectonic approaches. The fault sinks the northern sector of the Jiloca graben with respect to the Neogene infill of the Calatayud basin, both basins therefore being articulated as

two adjacent tilted steps (Fig. 1c). The fault trace trends NNW–SSE (N150° E in average) and is 18 km long, splitting into three or four nearly parallel branches in certain sectors (Figs. 3, 6a). Where the fault surfaces are exposed, they usually dip 70–75° E. Kinematical indicators observed in some of them in the central sector show nearly pure normal slip, with prevailing transport directions towards W and SW (mean slip vector towards N234° E reported at branch A; Fig. 11c).

The occurrence of older contractional structures near its northern sector (Liesa et al. 2021) suggests that the normal Calamocha fault resulted from inversion of a previous, Palaeogene to Early Miocene compressional structure, in the same way as it has been interpreted for the neighbouring Daroca Fault (Colomer and Santanach 1988; Casas et al. 2018). The onset of extensional activity has been documented in the Late Pliocene, 3.8 Ma ago.

The maximum normal throw at the northern and central sectors of the fault is in the range of 180–210 m, and the maximum net slip in the range of 190–230 m. The average long-term (3.8 Ma) slip rate has therefore been calculated to 0.05–0.06 mm/a.

Branches A and B at the central sector of the Calamocha fault have undergone recurrent slip during the Late Pleistocene, as evidenced by detailed study at three artificial exposures in the neighbourhoods of Calamocha town: Zaragoza–Sagunto railway (ZSR), Polígono Agroalimentario (PA), and the A-23 highway (A23H; Fig. 6a). A chronological synthesis of faulting episodes during the Pleistocene is depicted in Fig. 13. Site ZSR has provided a succession of four to five deformational events for branch A within the time lapse between  $145.9 \pm 9.1$  and  $68.9 \pm 5.2$  ka. Considering both scenarios (4 or 5 slip events), and seeing the age

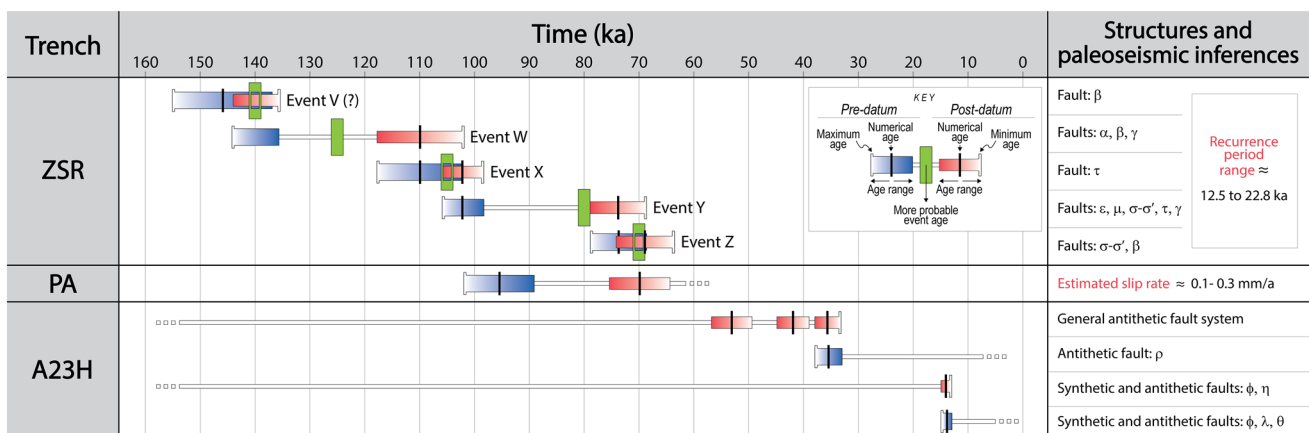


Fig. 13 Chronological summary of faulting events interpreted from trench study at branches A and B of the Calamocha fault



error bars, this results in an average recurrence period in the range of 12.5–22.8 ka. Site PA shows evidence of slip on branch A during/after the time lapse between  $95.4 \pm 6.3$  and  $69.9 \pm 5.5$  ka. Site A23H reveals that branch B has undergone slip events prior to  $53.1 \pm 3.7$ ,  $41.9 \pm 2.9$  and  $35.3 \pm 2.3$  ka, as well as others after  $35.3 \pm 2.3$  and  $13.8 \pm 0.9$  ka. Overall, (i) the ZSR trench records older deformation episodes; (ii) event Z in ZSR could be correlated with an indistinguishable fraction of the total fault slip recorded in PA (on the same fault branch A); (iii) the A23H slope has recorded imprecise faulting episodes, including the younger ones.

It is unfortunate that these data are not able to build a robust palaeoseismic succession for the Calamocha fault. Some of the deformation events interpreted in site ZSR do not represent visible accumulated displacement on the main fault; the slip balance on the ensemble of synthetic and antithetic faults is very small indeed (not much greater than 0.3 m). Only events W and Z could correspond to true slip episodes on fault branch A. Faulting episodes inferred at sites PA (branch A) and A23H (branch B) are not constrained enough in age for being correlated to build a complete evolutionary model. Nevertheless, from the available data, general notions can be retained about (i) the recurrent nature of deformation events since ca. 146 ka ago, (ii) their average recurrence period (12.5–22.8 ka for branch A), (iii) the slip rate (roughly estimated to 0.1–0.3 mm/a where visible slip has effectively accumulated; PA trench), and (iv) the proximity in time of the latest slip episodes (younger than 13.8 ka; Fig. 13).

These parameters definitely allow classifying the Calamocha fault as an active fault, according to most scientific classifications and legal regulations (e.g., NRC 1997; Machette 2000; Strom 2017). Moreover, the slip rate approached for a limited time window in the Late Pleistocene suggests that it has been higher than the long-term rate (0.1–0.3 mm/a vs. 0.05–0.06 mm/a).

## The Calamocha fault and associated deformation within the regional framework

The maximum net slip (190–230 m) and average slip rate (0.05–0.06 mm/a) reported for the last 3.8 Ma at the Calamocha fault are of the same order, but generally lower, than those of neighbouring faults in the region (Table 2).

The above-mentioned apparent increase of short-term (Late Pleistocene) with respect to the long-term (since Late Pliocene) slip rate that we have inferred for the Calamocha fault represents a common tendency in the central Iberian Chain (Table 2). Only for the E–W trending Valdecebro fault zone (transverse structure within the Teruel basin), the slip rate for the last 142 ka (0.05–0.07 mm/a) is similar to the long-term one (Simón et al. 2019). Nevertheless, it should be noted that such slip rate is partial, since it corresponds to a single fault branch among several branches active during the Late Pleistocene.

The same tendency towards an increasing slip rate had already manifested during Neogene times at the eastern margin of the Teruel basin, the main extensional macrostructure within the region. All things considered, the total slip rate (fault throw and associated bending) accommodated on distinct transects across the entire basin margin shows a similar value (0.07–0.09 mm/a). However, comparing both extensional episodes defined in the region, a clear increase has been evidenced: from 0.05 to 0.07 mm/a during Late Miocene to Early Pliocene times, to 0.12–0.16 mm/a during Late Pliocene–Quaternary times (Ezquerro et al. 2020).

Three contributing factors have been invoked by Ezquerro et al. (2020) for explaining such an increase in slip rate: (i) onshore, westwards propagation of extensional deformation from the inner parts of the Valencia Trough; (ii) onset of crustal doming at the central–eastern Iberian Chain, which induced the recent multidirectional tension; (iii) progressive fault linkage since the beginning of the Late Miocene.

**Table 2** Summary of net slip values and slip rates calculated for the Calamocha fault and other recent extensional faults within the central–eastern Iberian Chain

Fault	Net slip (m)	Long-term slip rate (mm/a) (3.8–3.5 Ma)	Short-term slip rate (mm/a)	References
Calamocha	190–230	0.05–0.06	0.1–0.3 (since 95.4–69.9 ka)	This work
Sierra Palomera	330–480	0.09–0.15		Peiro et al. (2022)
Concud	255–290	0.07–0.08	0.29 (since 74 ka)	Lafuente et al. (2011, 2014), Simón et al. (2016), Ezquerro et al. (2020)
Teruel	270	0.07	0.18–0.20 (since 46 ka)	Simón et al. (2017)
Valdecebro	190	0.05	0.05–0.07 (since 142 ka)	Simón et al. (2019)
Eastern margin of the Teruel basin	490–690	0.13–0.17		Ezquerro et al. (2020)
Río Grío–Pancrudo	260–325	0.07–0.09	0.3–0.36 (since 67 ka)	Peiro and Simón (2022)



The geometry and kinematics of the Calamocha fault are consistent with the recent tensional stress field, characterized by  $\sigma_3$  trajectories trending WSW–ENE (Simón 1982, 1989; Arlegui et al. 2005; Liesa et al. 2019). Most rupture surfaces observed in the surveyed outcrops are either closely parallel (sites ZSR and PA) or antithetic (site A23H) to the map-scale faults, but, in any case, they are parallel to the NNW–SSE trending  $S_{H_{max}}$  ( $\sigma_2$ ) stress trajectories. Therefore, all of them are favourably oriented to move as nearly pure normal faults, as the observed slickenlines indicate.

Nevertheless, the nature of the relationship between each fault branch and its subsidiary rupture surfaces, and hence the tectonic and palaeoseismic meaning of the latter, are different for each exposure studied. Faults are entirely synthetic with the main branch A in site PA, and mostly antithetic to branch B (associated with rollover kinematics of the hanging-wall block) in site A23H; however, in both cases, minor rupture surfaces are kinematically related to slip on the main faults. If the position and characteristics of Quaternary sediments linked to them would have made it possible to establish an almost complete succession of deformation events, their palaeoseismic significance would have been complete. This was not the case owing to: (i) the impossibility of identifying sedimentary units with distinct tectono-sedimentary relationships within Pleistocene sediments in site PA, and (ii) the laterally discontinuous occurrence of the colluvial deposits in site A23H. In the case of site ZSR, the quality of the available information has made it possible to reconstruct a succession of faulting episodes, but these cannot be directly linked to progressive slip of fault branch A. Consequently, we do not have direct information about the seismogenic behaviour of branch A, beyond overall perception on repeated deformation during the Late Pleistocene, with an average recurrence period in the order of  $10^1$  ka.

Relationships of the faulting succession interpreted at site ZSR with the Calamocha fault itself should not be sought at the kinematical level but at the dynamical level: both have a common origin within the regional stress framework. Maps of surface fractures resulting from large earthquakes (e.g., Philip and Meghraoui 1983; Lavecchia et al. 2012; Choi et al. 2019) reveal the structural complexity resulting from hierarchical development of (i) a large fault that propagates from the subsoil to the surface, (ii) subsidiary fractures and folds induced by the kinematics of the main fault, and (iii) accompanying faults directly controlled by the same regional stress field. The succession of faulting events at ZSR represents progressive deformation within the hanging-wall block of the Calamocha fault in response to the remote tensional stress field. The faulting succession indicates alternating slip on synthetic and antithetic faults, which has accommodated overall absolute horizontal stretching at this section of ca. 100 cm (local  $\beta$  factor = 1.1). The case is similar to the one

recently studied at a trench excavated in the hanging-wall block of the neighbouring Sierra Palomera fault (Peiro et al. 2022). It is not feasible that propagation or reactivation of those small ruptures occurred fully independently; more likely, it accompanied a major slip event in one of the main branches. Hence, although such minor faults do not directly represent a progressive slip of that fault, they have some palaeoseismological significance from a temporal point of view.

### Seismogenic characterization

According to the analysis carried out by Stirling et al. (2013) for the Global Earthquake Model (GEM), application of the regression model by Wesnousky (2008) is recommended for approaching seismogenic parameters in slow intraplate normal faults. Considering the length of the Calamocha fault trace (18 km) and the absence of structural segmentation, such regression provides a potential moment magnitude  $M_w = 6.7 \pm 0.3$  for earthquakes generated by this structure. This  $M_w$  value fits the range obtained from other common regression proposals (central values of  $M_w$  ranging from 6.3 to 6.9; Wells and Coppersmith 1994; Stirling et al. 2002; Leonard 2010), but should be regarded as more precise. Concerning the coseismic slip, despite the wide deviation bar that all regression models show, it should be noted that Wesnousky's (2008) model gives a potential average coseismic slip of ca. 0.5 m, while the other regressions (Wells and Coppersmith 1994; Stirling et al., 2002; Leonard 2010) point to values in the range of 0.4–2.2 m.

Testing the reliability of such values of coseismic slip is a difficult task since the results from our trench study are not robust enough, but they seem reasonably consistent. Some pieces of field information could provide an approach to the coseismic slip on individual branches of the Calamocha fault (“Seismogenic characterization”): (i) synthetic throws measured for two deformational events in trench ZSR (events W and Z; 0.45 and 0.5 m, respectively; Figs. 9b, 10); (ii) synthetic throw estimated for the hypothetical event V (> 0.5 m; Figs. 9b, 10); (iii) synthetic throw inferred from the rupture of colluvium Q4 along fault  $\phi$  in A23H (2.4 m; Fig. 12b). As explained above, Q4 had to undergo at least two deformation episodes, so the hypothesis that the 2.4 m throw in fault  $\phi$  was distributed among at least two events seems reasonable. From such premises, the average of estimated coseismic throws for events V, W, Z, and fault  $\phi$  would be in the range of 0.45–1.2 m, which approximately corresponds to net slip of 0.5–1.3 m (considering the orientation of fault planes and transport direction). Such quantities are within the range derived from the regressions mentioned above; we can therefore assume that they represent realistic values for the seismogenic behaviour of the Calamocha fault.

Once compiled and critically assumed the above information, it is also possible to calculate the potential moment

magnitude  $M_w$  by using the equation proposed by Hanks and Kanamori (1979), based on the notion of seismic moment  $M_0$ . For achieving such calculation, we have considered: (i) the average coseismic slip of 0.5–1.3 m; (ii) the rupture area expressed as the product of the trace length (18 km) and the fault width along dip (13–19 km, up to the regional detachment level, whose depth has been located by Roca and Guimerà 1992, and Ezquerro et al. 2020, at 11–17 km); (iii) the average shear modulus  $\mu$  commonly used for typical upper crustal rocks,  $3\text{--}3.5 \cdot 10^{10}$  Pa. The resulting  $M_w$  value lies in the range of 6.3–6.7. This  $M_w$  range lies within the aforementioned range estimated from regression models ( $M_w = 6.3\text{--}6.9$ ), so it can be assumed as the most accurate for the Calamocha fault.

Reliability of the other palaeoseismic parameters approached from trench study for Late Pleistocene times can be now assessed: slip rate of 0.1–0.3 mm/a (PA site), and average recurrence period of 12.5–22.8 ka (ZSR site). For both parameters, values in the lowest range are needed to be consistent with the formerly approached coseismic slip. Assuming a stick–slip fault regime at a rate of 0.1 mm/a, a recurrence period of 12.5 ka involves a coseismic slip of 1.25 m, which lies within the range estimated from field data (0.5–1.3 m), and also within that obtained from the regression models. Conversely, increasing the slip rate over 0.12 mm/a or the recurrence period over 15 ka would result in less realistic coseismic slip values. In summary, the following palaeoseismic parameters are adopted as the most probable and realistic for the Calamocha fault:  $M_w = 6.3\text{--}6.9$ ; coseismic slip = 0.5–1.3 m; recurrence period  $\leq 15$  ka; slip rate  $\approx 0.1$  mm/a.

An active fault able to produce earthquakes of  $M_w$  6.3–6.9 with recurrence period under 15 ka certainly represents a seismic source that should be considered in seismic hazard assessment of the region. Unfortunately, the incompleteness of the palaeoseismic data and, in particular, the lack of knowledge about the elapsed time, precludes the possibility of achieving a probabilistic assessment at this moment.

Finally, a scenario of rupture propagation along both the Calamocha and Daroca faults should not be ruled out. They are separated by a right relay zone 1.8 km wide (Figs. 1c, 3), which might not represent a barrier to propagation given their parallelism and favourable orientation with respect to the regional stress field. According to Biasi and Wesnousky (2016), 54% of relay zones  $\geq 1$  km wide, in dip-slip faults longer than 10 km, are overcome during fault propagation; moreover, such relay zones are less effective at stopping normal than reverse ruptures. If we consider the Calamocha–Daroca fault zone as a single structure 42 km long (27 km + 18 km – 3 km overlap), its complete rupture could generate earthquakes of magnitude  $6.9 \pm 0.3$ , according to the regression model by Wesnousky (2008).

## Conclusions

The Calamocha fault is a NNW–SSE striking, 70–75° E dipping, 18-km-long, nearly pure normal fault with an average transport direction (azimuth of the slip vector on the hanging-wall block) towards WSW. It was the result of the inversion of a previous compressional structure, in full coherence with the recent, WSW–ENE trending  $\sigma_3$  trajectories of the tensional stress field active since the Late Pliocene.

The maximum throw, recorded by a Late Pliocene planation surface (FES2, 3.8 Ma), is in the range of 180–210 m. This involves a maximum net slip of 190–230 m and slip rate of 0.05–0.06 mm/a since that age.

The Calamocha fault has undergone recurrent slip during the Late Pleistocene. On branch A, two artificial exposures have evidenced: (i) a probable slip event (V in ZSR site), with coseismic throw exceeding 0.5 m, dated to ca. 140 ka; (ii) two well-constrained slip events (W and Z), with coseismic throws of 0.45 and 0.5 m, dated to ca. 125 ka and ca. 70 ka, respectively; (iii) two other intercalated deformation events, dated to ca. 105 and 80 ka (X and Y), not explicitly linked to slip on the main fault; (iv) undifferentiated slip episodes that totalize net slip of 3.9–4.8 m (PA site) during/after the time lapse between  $95.4 \pm 6.3$  and  $69.9 \pm 5.5$  ka, one of them hypothetically correlated with event Z. Branch B has undergone (A23H site): (i) at least two slip episodes on the main rupture surface, totalizing a minimum throw of 2.2 m, older and younger, respectively, than  $13.8 \pm 0.9$  ka; (ii) undetermined events indirectly revealed by activation of antithetic faults prior to  $53.1 \pm 3.7$ ,  $41.9 \pm 2.9$  and  $35.3 \pm 2.3$  ka, and after  $35.3 \pm 2.3$  ka and  $13.8 \pm 0.9$  ka. The lack of Quaternary deposits affected by fault branch C prevents from knowing its recent activity.

The short-term slip rate has been roughly calculated to 0.1–0.3 mm/a for a narrow time window within the Late Pleistocene, although it should be estimated in the lowest range (ca. 0.1 mm/a) in order to fit realistic palaeoseismic parameters. In any case, it would be higher than the long-term rate, thus following the same tendency previously observed in most faults at the central Iberian Chain.

The seismogenic ability of the Calamocha fault is characterized by the following parameters: (i) potential moment magnitude  $M_w \approx 6.3\text{--}6.7$  ( $M_w \approx 6.6\text{--}7.2$  in a scenario of activation of the whole Calamocha–Daroca fault zone); (ii) average coseismic slip estimated in the range of 0.5–1.3 m; (iii) average recurrence period under 15 ka.

**Acknowledgements** The research has been financed by projects LMP127\_18 (Gobierno de Aragón–Programa Operativo del Fondo Europeo de Desarrollo Regional Aragón 2014–2020), and PID2019-108705-GB-I00 of the Agencia Estatal de Investigación (AEI/10.13039/501100011033) of the Spanish Government. This work is a contribution of the Geotransfer Research Group (E32\_20R) funded by Gobierno de Aragón. A. Peiro benefits from a FPU contract



(FPU17/02470) of the Spanish Government. We thank P. Benítez for the OSL dating at the Laboratorio de Datación y Radioquímica of the Universidad Autónoma de Madrid, as well as J. Brizuela for the drone photographs, and A. Whitehead for the English revision of the manuscript.

**Funding** Open Access funding provided thanks to the CRUE-CSIC agreement with Springer Nature.

**Open Access** This article is licensed under a Creative Commons Attribution 4.0 International License, which permits use, sharing, adaptation, distribution and reproduction in any medium or format, as long as you give appropriate credit to the original author(s) and the source, provide a link to the Creative Commons licence, and indicate if changes were made. The images or other third party material in this article are included in the article's Creative Commons licence, unless indicated otherwise in a credit line to the material. If material is not included in the article's Creative Commons licence and your intended use is not permitted by statutory regulation or exceeds the permitted use, you will need to obtain permission directly from the copyright holder. To view a copy of this licence, visit <http://creativecommons.org/licenses/by/4.0/>.

## References

- Adrover R (1986) Nuevas faunas de roedores en el Mio-Plioceno continental de la región de Teruel (España). Interés bioestratigráfico y paleoecológico. Instituto de Estudios Turolenses, Teruel
- Allen CR (1986) Seismological and paleoseismological techniques of research in active tectonics. In: Wallace RE (ed) Active tectonics studies in geophysics. National Academy Press, Washington, pp 148–154
- Álvoro M, Capote R, Vegas R (1979) Un modelo de evolución geotectónica para la Cadena Celtibérica. *Acta Geol Hisp* 14:172–177
- Anadón P, Moissenet E (1996) Neogene basins in the Eastern Iberian Range. In: Friend PF, Dabrio CF (eds) Tertiary basins of Spain. The stratigraphic Record of Crustal kinematics. World and Regional Geology series 6. Cambridge University Press, Cambridge, pp 68–76
- Anadón P, Alcalá L, Alonso-Zarza AM, Calvo JP, Ortí F, Rosell L, Sanz-Rubio E (2004) Cuencas de la Cordillera Ibérica. In: Vera JA (ed) Geología de España. Sociedad Geológica de España-Instituto Geológico y Minero, Madrid, pp 562–569
- Arlegui LE, Simón JL, Lisle RJ, Orife T (2005) Late Pliocene-Pleistocene stress field in the Teruel and Jiloca grabens (eastern Spain): contribution of a new method of stress inversion. *J Struct Geol* 27:693–705
- Bell WT (1979) Attenuation factors for the absorbed radiation dose in quartz inclusions for thermoluminescence dating. *Ancient TL* 8:1–12
- Biasi GP, Wesnousky SG (2016) Steps and gaps in ground ruptures: empirical bounds on rupture propagation. *Bull Seismol Soc Am* 106(3):1110–1124
- Calvín-Ballester P, Casas A (2014) folded variscan thrusts in the herera unit of the iberian range (NE Spain). *Geol Soc London Spec Publ* 394:39–52
- Capote R, Muñoz JA, Simón JL, Liesa CL, Arlegui LE (2002) Alpine tectonics I: the alpine system north of the Betic Cordillera. In: Gibbons W, Moreno T (eds) Geology of Spain. The Geological Society, London, pp 367–400
- Casas A, Marcén M, Calvín P, Gil A, Román-Berdiel T, Pocoví A (2016) Deformación varisca, tardivarisca y alpina en la Rama Aragonesa de la Cordillera Ibérica: propuesta para diferenciación y denominación de estructuras. *Geo-Temas* 16(2):495–498
- Casas AM, Gil A, Simón JL, Izquierdo E, Aldega L, Román T, Osácar C, Pueyo O, Ansón M, García C, Corrado S, Invernizzi C, Caricchi C (2018) Strain indicators and magnetic fabric in intraplate fault zones: case study of daroca thrust, Iberian Chain, Spain. *Tectonophysics* 730:29–47
- Choi JH, Ko K, Gihm YS, Cho CS, Lee H, Song SG, Bang ES, Lee HJ, Bae HK, Kim SW, Choi SJ, Lee SS, Lee SR (2019) Surface deformations and rupture processes associated with the 2017 Mw 5.4 Pohang, Korea, earthquake. *Bull Seismol Soc Am* 109(2):756–769
- Colomer M, Santanach P (1988) Estructura y evolución del borde sur-occidental de la Fosa de Calatayud-Daroca. *Geogaceta* 4:29–31
- Corral MB (2014) Estructura y relaciones tectónica-sedimentación en el contacto del Paleozoico de Villafeliche-Calamocha y la cuenca neógena de Calatayud. Universidad de Zaragoza, Trabajo Fin de Grado
- Cortés-Gracia A, Casas-Sainz AM (1996) Deformación alpina de zócalo y cobertera en el borde norte de la Cordillera Ibérica (Cubeta de Azuara-Sierra de Herrera). *Rev Soc Geol España* 9(1–2):51–66
- Durcan JA, King GE, Duller GAT (2015) DRAC: Dose rate and age calculator for trapped charge dating. *Quat Geochron* 28:54–61
- Ezquerro L (2017) El sector norte de la cuenca neógena de Teruel: tectónica, clima y sedimentación. PhD Thesis, Universidad de Zaragoza <http://zaguan.unizar.es/record/77098#>
- Ezquerro L, Lafuente P, Pesquero MD, Alcalá L, Arlegui LE, Liesa CL, Luque L, Rodríguez-Pascua MA, Simón JL (2012) Una cubeta endorreica residual del Pleistoceno inferior en la zona de relevo entre las fallas neógenas de Concud y Teruel, Cordillera Ibérica: implicaciones paleogeográficas. *Rev Soc Geol España* 25:157–175
- Ezquerro L, Moretti M, Liesa CL, Luzón A, Simón JL (2015) Seismites from a well core of palustrine deposits as a tool for reconstructing the palaeoseismic record of a fault. *Tectonophysics* 655:191–205
- Ezquerro L, Moretti M, Liesa CL, Luzón A, Pueyo E, Simón JL (2016) Controls on space-time distribution of soft-sediment deformation structures: applying palaeomagnetic dating to approach the apparent recurrence period of paleoseisms at the Concud fault (eastern Spain). *Sed Geol* 344:91–111
- Ezquerro L, Simón JL, Luzón A, Liesa CL (2020) Segmentation and increasing activity in the Neogene–Quaternary Teruel Basin rift (Spain) revealed by morphotectonic approach. *J Struct Geol* 135:104043. <https://doi.org/10.1016/j.jsg.2020.104403>
- Gabaldón V, Lendínez A, Ferreiro E, Ruiz V, López de Alda F, Valverde M, Lago San José M, Meléndez A, Pardo G, Ardevol L, Villena J, González A, Hernández A, Álvaro M, Leal M C, Aguilar Tomás M, Gómez JJ, Carls P. (1991) Mapa Geológico de España 1: 200.000, hoja nº 40 (Daroca). IGME, Madrid
- Galbraith RF, Roberts RG, Laslett GM, Yoshida H, Olley JM (1999) Optical dating of single and multiple grains of quartz from Jimmum rock shelter, Northern Australia: part 1, experimental design and statistical models. *Archaeometry* 41:339–364
- García-Lacosta AI, Pueyo Ó, Arlegui LE, Liesa CL, Ezquerro L, Simón JL (2014) La zona de falla reciente de Sierra Palomera (fosa del Jiloca, Cordillera Ibérica): contribución de la geofísica a la caracterización estructural. 2ª Reunión Ibérica sobre Fallas Activas y Paleoseismología-Iberfault (Lorca, Murcia), IGME, pp 51–54
- Gracia FJ (1992) Tectónica pliocena de la Fosa de Daroca (prov. de Zaragoza). *Geogaceta* 11:127–129
- Gracia FJ, Gutiérrez F, Gutiérrez M (2002) Origin and evolution of the Gallocanta polje (Iberian Range, NE Spain). *Z Geomorphol* 46:245–262
- Guerin G, Mercier N, Nathan R, Adamiec G, Lefrais Y (2012) On the use of the infinite matrix assumption and associated concepts: a critical review. *Radiat Meas* 47:778–785

- Gutiérrez M, Gracia FJ (1997) Environmental interpretation and evolution of the Tertiary erosion surfaces in the Iberian Range (Spain). *Geol Soc, London, Special Publ* 120(1):147–158
- Gutiérrez F, Gutiérrez M, Gracia FJ, McCalpin JP, Lucha P, Guerrero J (2008) Plio-Quaternary extensional seismotectonics and drainage network development in the central sector of the Iberian Chain (NE Spain). *Geomorphology* 102(1):21–42
- Gutiérrez F, Masana E, González A, Guerrero J, Lucha P, McCalpin JP (2009) Late quaternary paleoseismic evidence on the Munébrega Half-graben fault (Iberian Range, Spain). *Int J Earth Sci* 98:1691–1703. <https://doi.org/10.1007/s00531-008-0319-y>
- Gutiérrez F, Lucha P, Jordá L (2013) The Río Grío depression (Iberian Chain, NE Spain). Neotectonic graben vs. Fluvial Valley. *Cuaternario y Geomorfología* 27:5–32
- Gutiérrez F, Carbonel D, Sevil J, Moreno D, Linares R, Comas X, Zarroca M, Roqué C, McCalpin JP (2020a) Neotectonics and late holocene paleoseismic evidence in the Plio-Quaternary Daroca half-graben, Iberian Chain, NE Spain Implications for fault source characterization. *J Struct Geol* 131:103933
- Gutiérrez F, Moreno D, López GI, Jiménez F, del Val M, Alonso MJ, Martínez-Pillado V, Guzmán O, Martínez D, Carbonel D (2020b) Revisiting the slip rate of Quaternary faults in the Iberian Chain, NE Spain. *Geomorphol Seismic-Hazard Implic Geomorphol* 363:107233
- Hanks TC, Kanamori H (1979) A moment magnitude scale. *J Geophys Res* 84:2348–2350
- Hernández A, Olivé A, Moissenet E, Pardo G, Villena J, Portero JM, Gutiérrez M, Puigdefábregas C, Giner J, Aguilar MJ, Leal MC, Gutiérrez JC, Gil MD, Adrover R, Gabaldón V. (1983) Mapa Geológico de España 1: 50.000, Hoja nº 491 (Calamocha). IGME, Madrid
- Herraiz M, De Vicente G, Lindo-Ñaupari R, Giner J, Simón JL, González-Casado JM, Vadillo O, Rodríguez-Pascua MA, Cicuéndez JL, Casas A, Cabañas L, Rincón P, Cortés AL, Ramírez M, Lucini M (2000) The recent (upper Miocene to Quaternary) and present tectonic stress distributions in the Iberian Peninsula. *Tectonics* 19:762–786
- IGN (2022) Servicio de Información Sísmica del Instituto Geográfico Nacional. <https://www.ign.es/web/ign/portal/sis-catalogo-terremotos>
- Julivert M. (1954) Observaciones sobre la tectónica de la Depresión de Calatayud. Arrahona, Museo de Sabadell, pp 3–18
- Lafuente P, Arlegui LE, Liesa CL, Simón JL (2011) Paleoseismological analysis of an intraplate extensional structure: the Conclud fault (Iberian Chain, Eastern Spain). *Int J Earth Sci* 100:1713–1732
- Lafuente P, Arlegui LE, Liesa CL, Pueyo O, Simón JL (2014) Spatial and temporal variation of paleoseismic activity at an intraplate, historically quiescent structure: the Conclud fault (Iberian Chain, Spain). *Tectonophysics* 632:167–187
- Lavecchia G, de Nardis R, Cirillo D, Brozzetti F, Boncio P (2012) The May–June 2012 Ferrara Arc earthquakes (northern Italy): structural control of the spatial evolution of the seismic sequence and of the surface pattern of coseismic fractures. *Ann Geophys.* <https://doi.org/10.4401/ag-6173>
- Leonard M (2010) Earthquake fault scaling: self-consistent relating of rupture length, width, average displacement, and moment release. *Bull Seismol Soc Am* 100(5A):1971–1988
- Liesa CL, Simón JL (2009) Evolution of intraplate stress fields under multiple compressions: The case of the Iberian Chain (NE Spain). *Tectonophysics* 474:144–159
- Liesa CL, Simón JL, Casas AM (2018) La tectónica de inversión en una región intraplaca: La Cordillera Ibérica. *Rev Soc Geol España* 31:23–50
- Liesa CL, Simón JL, Ezquerro L, Arlegui LE, Luzón A (2019) Stress evolution and structural inheritance controlling an intracontinental extensional basin: the central-northern sector of the Neogene Teruel Basin. *J Struct Geol* 118:362–376
- Liesa CL, Corral MB, Arlegui LA, Peiro A, Simón JL. (2021) Inversión tectónica negativa y estructuración de la zona de relevo entre las fallas normales plio-cuaternarias de Calamocha y Daroca. X Congreso de Geología de España, Sociedad Geológica de España, Vitoria, Spain
- Liu L, Zoback MD (1997) Lithospheric strength and intraplate seismicity in the New Madrid seismic zone. *Tectonics* 16(4):585–595
- Maillard A, Mauffret A (1999) Crustal structure and riftogenesis of the Valencia Trough (north-western Mediterranean Sea). *Basin Res* 11(4):357
- McCalpin J (2009) *Paleoseismology*, 2nd edn. Academic Press
- Machette MN (2000) Active, capable, and potentially active faults—a paleoseismic perspective. *J Geodyn* 29:387–392
- Martín-Bello L, Arlegui LE, Ezquerro L, Liesa CL, Simón JL. (2014) La falla de Calamocha (fosa del Jiloca, Cordillera Ibérica): estructura y actividad pleistocena. 2ª Reunión Ibérica sobre Fallas Activas y Paleosismología-Iberfault (Lorca, Murcia), IGME, pp 55–85
- Moissenet E (1980) Relief et déformations récentes: trois transversales dans les fossés internes des chaînes Ibériques orientales. *Revue De Géographie Des Pyrenées Et Sud-Ouest* 51:315–344
- NRC (1997) Regulatory Guide 1.165, Identification and Characterization of Seismic Sources and Determination of Safe Shutdown Earthquake Ground Motions US. Nuclear Regulatory Commission, Office of Nuclear Regulatory Research, Washington
- Peiro A, Simón JL (2021a) Caracterización preliminar de la zona de falla de Río Grío-Pancrudo: estructura extensional de primer orden en la evolución reciente de la Cordillera Ibérica. *Geo-Temas* 18:846–849
- Peiro A, Simón JL (2021b) The Río Grío-Pancrudo Fault Zone (central Iberian Chain, Spain): recent extensional activity revealed by drainage reversal. *Geol Mag* 159:21–36. <https://doi.org/10.1017/S0016756821000790>
- Peiro A, Simón JL, Román-Berdiel T (2020) Fault relay zones evolving through distributed longitudinal fractures: the case of the Teruel graben system (Iberian Chain, Spain). *J Struct Geol* 131:103942. <https://doi.org/10.1016/j.jsg.2019.103942>
- Peiro A, Simón JL, Arlegui LE, Ezquerro L, García-Lacosta AI, Lameillas MT, Liesa CL, Luzón A, Martín-Bello L, Pueyo-Anchuela Ó, Russo N (2022) Hanging-wall deformation at the active Sierra Palomera extensional fault (Jiloca basin, Spain) from structural, morphotectonic, geophysical and trench study. *Tectonophysics* 828:229274
- Peña JL, Gutiérrez M, Ibáñez M, Lozano MV, Rodríguez J, Sánchez M, Simón JL, Soriano MA, Yetano LM. (1984) Geomorfología de la provincia de Teruel. Instituto de Estudios Turolenses, Teruel
- Philip H, Meghraoui M (1983) Structural analysis and interpretation of the surface deformations of the El Asnam earthquake of October 10, 1980. *Tectonics* 2(1):17–49
- Prescott JR, Hutton JT (1994) Cosmic ray contributions to dose rates for luminescence and ESR: large depths and long-term time variations. *Radiat Meas* 23:497–500
- Roca E, Guimerà J (1992) The Neogene structure of the eastern Iberian margin: structural constraints on the crustal evolution of the Valencia trough (western Mediterranean). *Tectonophysics* 203:203–218
- Rubio JC. (2004) Los humedales del Alto Jiloca: estudio hidrogeológico e histórico-arqueológico. Consejo de Protección de la Naturaleza de Aragón, Zaragoza
- Rubio JC, Simón JL (2007) Tectonic subsidence vs. erosional lowering in a controversial intramontane depression: the Jiloca basin (Iberian Chain, Spain). *Geol Mag* 144:1–15



- Rubio JC, Simón JL, Soriano A (2007) Interacting tectonics, hydrogeology and karst processes in an intramontane basin: the Jiloca graben (NE Spain). *Hydrogeol J* 15:1565–1576
- Sanz-Rubio E (1999) Análisis de los sistemas deposicionales carbonáticos y evaporíticos del Neógeno de la Cuenca de Calatayud (provincia de Zaragoza). PhD Thesis, Universidad Complutense de Madrid
- Sanz-Rubio E, Sánchez-Moral S, Cañaveras JC, Abdul-Aziz H, Calvo JP, Cuezva S, Mazo AV, Rouchy JM, Sesé C, Van Darn J (2003) Síntesis de la cronoestratigrafía y evolución sedimentaria de los sistemas lacustres evaporíticos y carbonatados neógenos de la cuenca de Calatayud–Montalbán. *Estud Geol* 59:83–105
- Schwartz DP, Coppersmith KJ (1984) Fault behavior and characteristic earthquakes: examples from Wasatch and San Andreas fault zones. *J Geophys Res* 89:5681–5698
- Simón JL (1982) Compresión y distensión alpinas en la Cadena Ibérica Oriental. PhD Thesis, Universidad de Zaragoza (publ. Instituto de Estudios Turolenses, Teruel, 1984)
- Simón JL (1983) Tectónica y neotectónica del sistema de fosas de Teruel. *Teruel* 69:21–97
- Simón JL (1989) Late Cenozoic stress field and fracturing in the Iberian Chain and Ebro Basin (Spain). *J Struct Geol* 11:285–294
- Simón JL, Arlegui L, Lafuente P, Liesa CL (2012) Active extensional faults in the central–eastern Iberian Chain, Spain. *J Iber Geol* 38:127–144
- Simón JL, Arlegui LE, Ezquerro L, Lafuente P, Liesa CL, Luzón A (2016) Enhanced paleoseismic succession at the Conclud Fault (Iberian Chain, Spain): new insights for seismic hazard assessment. *Na Hazards* 80(3):1967–1993
- Simón JL, Arlegui LE, Ezquerro L, Lafuente P, Liesa CL, Luzón A (2017) Assessing interaction of active extensional faults from structural and paleoseismological analysis: the Teruel and Conclud faults (eastern Spain). *J Struct Geol* 103:100–119
- Simón JL, Ezquerro L, Arlegui LE, Liesa CL, Luzón A, Medialdea A, García A, Zarazaga D (2019) Role of transverse structures in paleoseismicity and drainage rearrangement in rift systems: the case of the Valdecebro fault zone (Teruel graben, eastern Spain). *Int J Earth Sci* 108:1429–1449. <https://doi.org/10.1007/s00531-019-01707-9>
- Simón JL, Casas-Sainz AM, Gil-Imaz A (2021) Controversial epiglyptic thrust sheets: the case of the daroca thrust (Iberian Chain, Spain). *J Struct Geol* 145:104298
- Simón-Porcar G, Liesa CL, Simón JL (2019) La cuenca neógena extensional de El Pobo (Teruel, Cordillera Ibérica): sedimentología, estructura y relación con la evolución del relieve. *Revista De La Sociedad Geológica De España* 32:17–42
- Sinusía C, Pueyo EL, Azanza B, Pocoví A (2004) Datación magnetoestratigráfica del yacimiento paleontológico de la Puebla de Valverde (Teruel). *Geo-Temas* 6(4):339–342
- Stirling M, Rhoades D, Berryman K (2002) Comparison of earthquake scaling relations derived from data of the instrumental and preinstrumental era. *Bull Seismol Soc Am* 92(2):812–830
- Stirling M, Goded T, Berryman K, Litchfield N (2013) Selection of earthquake scaling relationships for seismic-hazard analysis. *Bull Seismol Soc Am* 103(6):2993–3011
- Strom A. (2017) Active faults at structure's foundations: Definition and its influence on hazard assessment. Proceedings 16th World Conference on Earthquake Engineering, Santiago de Chile
- Vegas R, Fontboté JM, Banda E (1979) Widespread Neogene rifting superimposed on alpine regions of the Iberian Peninsula. Proceedings Symposium Evolution and Tectonics of the Western Mediterranean and Surrounding Areas, EGS, Viena, Instituto Geográfico Nacional, Madrid, Special Publ 201:109–128
- Wells DL, Coppersmith KJ (1994) New empirical relationships among magnitude, rupture length, rupture width, rupture area, and surface displacement. *Bull Seismol Soc Am* 84:974–1002
- Wesnousky SG (2008) Displacement and geometrical characteristics of earthquake surface ruptures: Issues and implications for seismic-hazard analysis and the process of earthquake rupture. *Bull Seismol Soc Am* 98(4):1609–1632
- Wintle AG (1997) Luminescence dating: laboratory procedures and protocols. *Radiat Meas* 27:769–817
- Yeats RS, Sieh K, Allen CR (1997) The geology of earthquakes. Oxford University Press, New York